

2009

## Nanostructure morphology variation modeling and estimation for nanomanufacturing process yield improvement

Gang Liu  
*University of South Florida*

Follow this and additional works at: <https://digitalcommons.usf.edu/etd>



Part of the [American Studies Commons](#)

---

### Scholar Commons Citation

Liu, Gang, "Nanostructure morphology variation modeling and estimation for nanomanufacturing process yield improvement" (2009). *USF Tampa Graduate Theses and Dissertations*.  
<https://digitalcommons.usf.edu/etd/2064>

This Thesis is brought to you for free and open access by the USF Graduate Theses and Dissertations at Digital Commons @ University of South Florida. It has been accepted for inclusion in USF Tampa Graduate Theses and Dissertations by an authorized administrator of Digital Commons @ University of South Florida. For more information, please contact [digitalcommons@usf.edu](mailto:digitalcommons@usf.edu).

Nanostructure Morphology Variation Modeling and Estimation for  
Nanomanufacturing Process Yield Improvement

by

Gang Liu

A thesis submitted in partial fulfillment  
of the requirements for the degree of  
Master of Science in Industrial Engineering  
Department of Industrial and Management Systems Engineering  
College of Engineering  
University of South Florida

Co-Major Professor: Qiang Huang, Ph.D.  
Co-Major Professor: José Zayas-Castro, Ph.D.  
Michael Weng, Ph.D.

Date of Approval:  
October 30, 2009

Keywords: nanowire, Gaussian Markov random field, neighborhood structure,  
interaction, autoregressive scheme

© Copyright 2009, Gang Liu

## **Acknowledgements**

First and foremost, I would like to express my sincere gratitude to Dr. Qiang Huang for his instantly inspiring guidance, hearty encouragement, valuable advices and constant support through the entire course of this study. I appreciate him so much for providing me this great opportunity to work in the Nanomanufacturing Quality Control Lab and introducing me to the new world.

Secondly, special thanks for Dr. José Zayas-Castro and Dr. Michael Weng for being my committee members and for the excellent suggestions they proposed in my defense and for my thesis.

Next, thanks are given to the students from Advanced Materials Research Lab. Dr. Qiang Hu and Farah Alvi helped me to much extent with the experimentation and scanning electron microscopy images collection.

Thanks also go to my friends here, who give me sincere suggestions on the research work and help me with my study and life. The names especially need to be mentioned are: Xi Zhang, Hui Wang, Shaoqiang Chen, Yang Tan, Qingwei Li and Yu An from industrial and system management engineering department. I should also say thanks to L. Xu who helped with the proof of absolute term.

I gratefully acknowledge the financial support from NSF.

Finally, I am heavily indebted to my parents, Q.W. Liu and X.Y. Xiang, who have been firmly supporting me and encouraging me from the behind. I would like to express my great appreciation and love to them.

## Table of Contents

|  |     |
|--|-----|
| List of Tables   | iii |
| List of Figures  | iv  |
| Abstract   | v   |
| Chapter 1 Introduction and Background                          | 1   |
| 1.1 Introduction to Nanotechnology                             | 1   |
| 1.1.1 Features at Nanoscale                                    | 2   |
| 1.1.2 Applications of Nanotechnology                           | 3   |
| 1.2 Introduction to Nanowire                                   | 5   |
| 1.2.1 Features of Nanowire                                     | 6   |
| 1.2.2 Quantum Confinement                                      | 7   |
| 1.2.3 Classifications of Nanowire                              | 8   |
| 1.2.3.1 Silicon Nanowire                                       | 8   |
| 1.2.3.2 ZnO Nanowire   | 10  |
| 1.2.3.3 Silica Nanowire  | 12  |
| 1.2.3.4 III-IV Semiconducting Nanowire                         | 13  |
| 1.3 Nanowire-Growth Process                                    | 14  |
| 1.3.1 Physical Vapor Deposition Method                         | 14  |
| 1.3.2 Chemical Vapor Deposition                                | 16  |
| 1.3.3 Solution-Based Chemical Synthesis Methods                | 17  |
| 1.4 Nanowire Growth Kinetics                                   | 17  |
| 1.5 Challenges of Current Nanomanufacturing Process            | 20  |
| 1.6 Research Objectives  | 21  |
| 1.7 Thesis Structure   | 22  |
| 1.8 Summary  | 22  |
| Chapter 2 Experimental Methods and Characterization Techniques | 23  |
| 2.1 Introduction to Experiment System                          | 23  |
| 2.2 Characterization Techniques                                | 24  |
| 2.2.1 Scanning Electron Microscopy                             | 25  |
| 2.2.2 Nanowire Length Measurement Development                  | 27  |
| 2.2.3 Results and Data Tables                                  | 30  |
| 2.3 Summary  | 33  |
| Chapter 3 Nanostructure Morphology Variation Modeling          | 34  |
| 3.1 Space-Time Random Field Model of Nanostructure Morphology  | 34  |
| 3.2 Motivation of Modeling via Gaussian Markov Random Fields   | 35  |
| 3.3 Modeling of Nanowire Morphology Variation                  | 36  |
| 3.4 Construction of Precision Matrix of GMRFs                  | 38  |
| 3.4.1 Precision Matrix for Infinite Lattice                    | 38  |

|   |    |
|---|----|
| 3.4.1.1 Conditional Autoregression Scheme                               | 38 |
| 3.4.1.2 Simultaneous Autoregressive Scheme                              | 39 |
| 3.4.2 Precision Matrix for Finite Lattice                               | 40 |
| 3.5 The Simulation of Morphology Variation by Improper GMRF             | 43 |
| 3.6 Summary   | 45 |
| Chapter 4 Parameters Estimation for Nanowire Morphology Variation Model | 46 |
| 4.1 Autoregressive Scheme   | 46 |
| 4.2 Simultaneous Autoregressive Scheme and the Increments               | 47 |
| 4.3 Maximum-Likelihood Estimation for Autoregressive Schemes            | 47 |
| 4.4 Coding Methods on Lattice   | 50 |
| 4.5 Parameter Estimation Method Using Simulation Data                   | 52 |
| 4.6 Model Estimation for Two Sets of Real Data                          | 53 |
| 4.7 Summary   | 58 |
| Chapter 5 Conclusions   | 59 |
| References  | 61 |

## List of Tables

|         |   |    |
|---------|---|----|
| Table 1 | Data of Lengths for the First Set of Nanowires      | 31 |
| Table 2 | Data of Lengths for the Second Set of Nanowires     | 32 |
| Table 3 | Data Simulated from the Model with Given Parameters | 53 |
| Table 4 | Parameters Estimation for Data Set 3 under by MLE   | 53 |
| Table 5 | Parameters Estimation for Data Set 1 under by MLE   | 54 |
| Table 6 | Parameters Estimation for Data Set 1 under by MLE   | 55 |
| Table 7 | Parameters Estimation for Data Set 2 under by MLE   | 56 |
| Table 8 | Parameters Estimation for Data Set 2 under by MLE   | 56 |

## List of Figures

|        |   |    |
|--------|---|----|
| Fig.1  | The Four Forms of Nanostructures                                | 5  |
| Fig.2  | A Diagram for ZnO Nanowires Synthesis                           | 24 |
| Fig.3  | Interactions of Electrons with the Sample                       | 25 |
| Fig.4  | Electron Interactions with Specimen-Scattering Events           | 26 |
| Fig.5  | SEM Image at the Magnification of 12K                           | 27 |
| Fig.6  | ZnO Nanowires of the Same Region Observed from Different Angles | 28 |
| Fig.7  | The Position Change of the Same Nanowire after the Rotation     | 28 |
| Fig.8  | The Two Sets of the Observed Nanowires                          | 30 |
| Fig.9  | Morphology Variation from the Data Set 1                        | 31 |
| Fig.10 | Morphology Variation from the Data Set 2                        | 32 |
| Fig.11 | A 3 by 3 Lattice of Local Variability                           | 41 |
| Fig.12 | Simulation for Central Increments                               | 43 |
| Fig.13 | Simulation for Forward Increments with Interactions             | 44 |
| Fig.14 | Simulation for Forward Increments without Interactions          | 44 |
| Fig.15 | Simulation for Increments from Spatial Statistics               | 45 |
| Fig.16 | Coding Pattern for a First-order Scheme                         | 50 |
| Fig.17 | Coding Pattern for a Second-order Scheme                        | 51 |

# **Nanostructure Morphology Variation Modeling and Estimation for Nanomanufacturing Process Yield Improvement**

Gang Liu

## **ABSTRACT**

Nanomanufacturing is critical to the future growth of U.S. manufacturing. Yet the process yield of current nanodevices is typically 10% or less. Particularly in nanomaterials growth, there may exist large variability across the sites on a substrate, which could lead to variability in properties. Essential to the reduction of variability is to mathematically describe the spatial variation of nanostructure.

This research therefore aims at a method of modeling and estimating nanostructure morphology variation for process yield improvement. This method consists of (1) morphology variation modeling based on Gaussian Markov random field (GMRF) theory, and (2) maximum likelihood estimation (MLE) of morphology variation model based on measurement data. The research challenge lies in the proper definition and estimation of the interactions among neighboring nanostructures.

To model morphology variation, nanostructures on all sites are collectively described as a GMRF. The morphology variation model serves for the space-time growth model of nanostructures. The probability structure of the GMRF is specified by a so-called simultaneous autoregressive scheme, which defines the neighborhood systems for any site on a substrate. The neighborhood system characterizes the interactions among adjacent nanostructures by determining neighbors and their influence on a given site in terms of conditional auto-regression. The conditional

auto-regression representation uniquely determines the precision matrix of the GMRF. Simulation of nanostructure morphology variation is conducted for various neighborhood structures. Considering the boundary effects, both finite lattice and infinite lattice models are discussed.

The simultaneous autoregressive scheme of the GMRF is estimated via the maximum likelihood estimation (MLE) method. The MLE estimation of morphology variation requires the approximation of the determinant of the precision matrix in the GMRF. The absolute term in the double Fourier expansion of a determinant function is used to approximate the coefficients in the precision matrix. Since the conditional MLE estimates of the parameters are affected by coding the data, different coding schemes are considered in the estimation based on numerical simulation and the data collected from SEM images. The results show that the nanostructure morphology variation modeling and estimation method could provide tools for yield improvement in nanomanufacturing.

## **Chapter 1**

### **Introduction and Background**

In this introductory chapter, the broad background of the research work, nanotechnology, and the relatively narrow background of the research work, nanowire, will be discussed respectively and successively. After the classification of nanowire, the growth process and the growth kinetics of nanowire will be introduced. Later sections deal with challenges of the current nanomanufacturing process and the robust design of nanowire synthesis to improve the yield of the nanomanufacturing process. The research work aims to improve the yields of the nanomanufacturing process by modeling the morphology variation of nanowire. This motivation is directly from the common challenges in the nanomanufacturing process. The statement of research objective and the significance of the research follow the motivation. The chapter concludes with the structure of the thesis.

#### **1.1 Introduction to Nanotechnology**

The term "nanotechnology" has evolved over the years via terminology drift to mean "anything smaller than microtechnology," such as nano powders, and other things that are nanoscale in size, but not referring to mechanisms that have been purposefully built from nanoscale components. Nanotechnology actually refers to the science and engineering of materials, structures and devices in which at least one of the dimensions is 100 nm or less. In a broader perspective, nanotechnology also includes the fabrication techniques in which objects are designed and built by the specification and placement of individual atoms or molecules both in an additive and subtractive manner.

An accredited definition of nanotechnology by NNI (National Nanotechnology Initiative) is the understanding and control of matter at dimensions of roughly 1 to 100 nanometers, where unique phenomena enable novel applications. Encompassing nanoscale science, engineering and technology, nanotechnology involves imaging, measuring, modeling, and manipulating matter at this length scale.

### **1.1.1 Features at Nanoscale**

Because the nanostructures are very tiny in size, they have salient features at nanoscale dimensions as follows [1].

Firstly, the dimensions of nanostructures are comparable to the size of biomolecules (such as proteins, Vander Waal's force, pharmokinetics, surface dynamics, and diffusion and transport mechanisms). Such an attribute makes them as sensitive probes to unravel atomistic and molecular events with great accuracy.

Secondly, the ratio of the surface area to total volume is a direct measure of reactivity for any system/material. When the volume is too large relative to surface area, diffusion cannot occur at sufficiently high rates as molecules/particles take time to reach the active surface. An increased surface area to volume ratio means increased exposure to the environment, which in turn translates as a sensitive surface to minor surface perturbations. In addition, a high surface area to volume ratio provides the required acceleration to negotiate thermodynamic barriers, thereby minimizing free energy. Also, nanostructures possess high surface to volume ratio facilitating faster diffusion mechanism.

Thirdly, one and two-dimensional nanostructures are generally high-aspect ratio (ratio of length to diameter) arrangements with directionality-dependent (along various axes) material properties. For example, (a) the deflection or absorbance of incident light would vary with the texture of the nanostructures, (b) a mechanical

property like Young's Modulus or (c) a magnetic property like hysteresis would change with orientation. Also, the nanostructures could be tuned to achieve desired material attributes leveraging size dependent characteristics.

Active surface is another key feature. The diminutive sizes of nanoscale materials enable (a) the entry of foreign materials through adsorption and diffusion, (b) specific chemical interaction, and (c) physisorption by acting as templates. Collectively coining the above-mentioned feature as 'Doping and Fictionalizations', nanostructures present an active surface for implementing various applications.

Finally, the advancements in semiconductor manufacturing in combination with precision metrology have enabled high-density synthesis of nanostructures at a faster rate to achieve the real promise of developing and manufacturing new nanomaterials, devices, and products in a cost-effective manner.

### **1.1.2 Applications of Nanotechnology**

Because nanotechnology is essentially a set of techniques that allow manipulation of properties at a very small scale, it can have many applications [2].

The first application is in drug delivery. Today, most harmful side effects of treatments such as chemotherapy are a result of drug delivery methods that don't pinpoint their intended target cells accurately. Researchers at Harvard and MIT have been able to attach special RNA strands, measuring about 10 nm in diameter, to nanoparticles and fill the nanoparticles with a chemotherapy drug. These RNA strands are attracted to cancer cells. When the nanoparticle encounters a cancer cell it adheres to it and releases the drug into the cancer cell. This directed method of drug delivery has great potential for treating cancer patients while producing fewer harmful side effects than those produced by conventional chemotherapy.

The second application relates to fabrics. The properties of familiar fabrics are being changed by manufacturers who are adding nano-sized components to conventional materials to improve performance. For example, some clothing manufacturers are making water and stain repellent clothing using nano-sized whiskers in the fabric that cause water to bead up on the surface.

A third use of nanotechnology deals with the reactivity of materials. The properties of many conventional materials change when formed as nano-sized particles (nanoparticles). This is generally because nanoparticles have a greater surface area per weight than larger particles; they are therefore more reactive to some other molecules. For example, studies have shown that nanoparticles of iron can be effective in the cleanup of chemicals in groundwater because they react more efficiently to those chemicals than larger iron particles.

Nanotechnology has also been applied to improve the strength of materials. Nano-sized particles of carbon (for example nanotubes and bucky balls) are extremely strong. Nanotubes and bucky balls are composed of only carbon and their strength comes from special characteristics of the bonds between carbon atoms. One proposed application that illustrates the strength of nanosized particles of carbon is the manufacture of t-shirt weight bullet proof vests made out of carbon nanotubes.

Another application of nanotechnology is in Micro/Nano ElectroMechanical Systems. The ability to create gears, mirrors, sensor elements, as well as electronic circuitry in silicon surfaces allows the manufacture of miniature sensors such as those used to activate the airbags in your car. This technique is called MEMS (Micro-ElectroMechanical Systems). The MEMS technique results in close integration of the mechanical mechanism with the necessary electronic circuit on a single silicon chip, similar to the method used to produce computer chips. Using

MEMS to produce a device reduces both the cost and size of the product, compared to similar devices made with conventional methods. MEMS is a stepping stone to NEMS or Nano-ElectroMechanical Systems. NEMS products are being made by a few companies, and will take over as the standard once manufacturers make the investment in the equipment needed to produce nano-sized features.

Molecular Manufacturing also involves nanotechnology now. If you're a Star Trek fan, you remember the replicator, a device that could produce anything from a space age guitar to a cup of Earl Grey tea. Your favorite character just programmed the replicator, and whatever he or she wanted appeared. Researchers are working on developing a method called molecular manufacturing that may someday make the Star Trek replicator a reality. The gadget these folks envision is called a molecular fabricator; this device would use tiny manipulators to position atoms and molecules to build an object as complex as a desktop computer. Researchers believe in the future it may be possible to reproduce almost any inanimate object using this method.

## 1.2 Introduction to Nanowire

Based on the structure and morphology of the nanostructures, the nanocomponents can be broadly classified as nanoparticles, nanowires/nanorods, nanotubes and nano – thin films, as shown on Fig.1 [3].

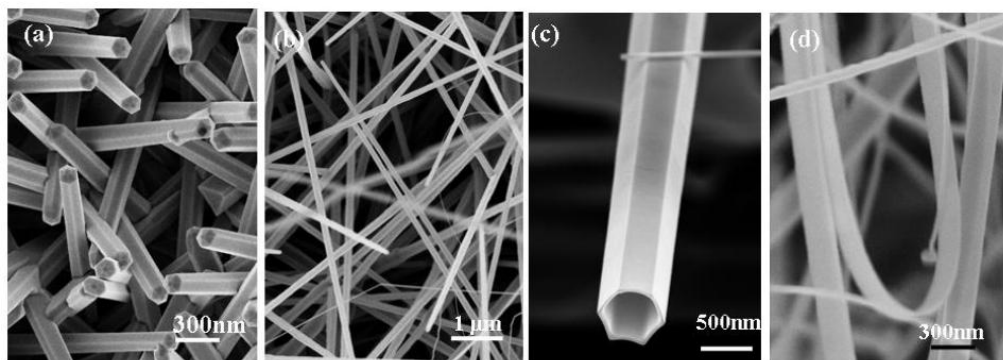


**Fig.1 The Four Forms of Nanostructures**

Among the several nanocomponents, nanowires have been preferred for many functional applications due to their efficient transport of electrons, structural anisotropy and the possibility of quantum confinement.

### **1.2.1 Features of Nanowire**

A nanowire is a nanostructure, with the diameter of the order of a nanometer. Alternatively, nanowires can be defined as structures that have a thickness or diameter constrained to tens of nanometers or less and an unconstrained length.

The conductivity of a nanowire is expected to be much less than that of the corresponding bulk material. This is due to a variety of reasons. First, there is scattering from the wire boundaries, when the wire width is below the free electron mean free path of the bulk material. In copper, for example, the mean free path is 40 nm. Nanowires less than 40 nm wide will shorten the mean free path to the wire width. Nanowires also show other peculiar electrical properties due to their size. Unlike carbon nanotubes, whose motion of electrons can fall under the regime of ballistic transport (meaning the electrons can travel freely from one electrode to the other), nanowire conductivity is strongly influenced by edge effects. The edge effects come from atoms that lay at the nanowire surface and are not fully bonded to neighboring atoms like the atoms within the bulk of the nanowire. The unbonded atoms are often a source of defects within the nanowire, and may cause the nanowire to conduct electricity more poorly than the bulk material. As a nanowire shrinks in size, the surface atoms become more numerous compared to the atoms within the nanowire, and edge effects become more important.

Due to their high Young's moduli, their use in mechanically enhancing composites is being investigated. Because nanowires appear in bundles, they may be

used as tribological additives to improve friction characteristics and reliability of electronic transducers and actuators.

### **1.2.2 Quantum Confinement**

Quantum confinement is a unique phenomenon observed in nanowires which has been exploited to alter the electronic properties for application specific requirements. Quantum confinement describes the organization of energy levels into which electrons can transverse when excited and becomes more relevant when the exciton (electron-hole pair) has squeezed into a dimension that approaches a critical quantum measurement, called the exciton Bohr radius. Physical separation between an electron and hole constitutes the Bohr radius which varies with different substances. The confinement phenomenon is better understood taking into consideration the quantum mechanics behind it. Electrons and holes or in general particles are considered to possess wave like properties described by a spatial wave function. Constraining them in a small space indicates only particular types of wave-function are allowed. Each must be exactly the right length and shape to satisfy the Schrödinger wave equation while under the effect of the trap. The solution to the wave equation corresponds to a particular characteristic length as well as a particular energy to form a "ladder", with higher rungs corresponding to higher energy.

When the confining dimension is large compared to the wavelength of the particle, the particle behaves freely with continuum energy levels. As the confining dimension decreases, the particle's energy increases discretely. This can be further explained by the photoluminescence phenomenon (process in which material absorbs photons and re-emits photons of characteristic wavelength). The energy of the emitted light is governed by the material composition in the case of a bulk semiconductor. When the physical size of the semiconductor is considerably reduced to be much

smaller than the Bohr radius, additional energy is required to confine this excitation within the nanoscopic structure leading to a shift in the emission to shorter wavelengths. Since the electron is given a wave treatment, conventional law such as Ohm's law doesn't hold at nanoscale. In the macroscopic world, Au is a better conductor than Pb; however, in atomic scale conduction Pb underpins Au by three orders of magnitude.

The significance of Quantum Confinement is reflected by the following two aspects: I) It increases the efficiency and performance of devices. Conventional lasers are created with thin film epitaxial of III-V semiconductors. Though the bulk of modern lasers are highly functional and reliable, they are inefficient in terms of energy consumption and heat dissipation. Adopting 1-D nanowires or 0-D quantum dots enables higher efficiencies and brighter lasers with the possibility of on-chip integration. II) External environment can manipulate the devices as well. The discrete energy levels in a nanowire could easily be altered by changing the environment such as a changing the electric and magnetic field or the introduction of a dielectric interface. Quantum dots/particles/wires can be easily manipulated precisely by STM or AFM generated fields.

### **1.2.3 Classifications of Nanowire**

Based on the electrical conductivity of the nanowires, they are broadly classified as metallic and semiconducting. Some of the reported configurations of metallic nanowires are that of Au, Ag, Ni, Pd and Co, while Si, ZnO, SnO<sub>2</sub>, GaN and SiO<sub>2</sub> forms the repertoire of semiconducting nanowires.

#### **1.2.3.1 Silicon Nanowire**

Silicon (Si) is the second most abundant element in the earth's crust, and its versatility in many applications is imparted by the semiconductor manufacturing

industry which has developed the standardized infrastructure and the technical ‘know-how’ to process it. However, though Si is configured as a mechanical material for microstructures, its indirect band gap ( $\sim 1.1\text{eV}$ ), making it a poor light emitter. The development of efficient light-emitting silicon devices or structures would enable optical interconnect on a new generation of chips. Hence, the research thrust was to engineer silicon to enhance its properties. One such effort led to the synthesis of Si nanowires. Many techniques have been applied to synthesize Si nanowires, ranging from laser ablation methods to solution techniques [4, 5]. Routinely, ordered arrays of vertically aligned Si nanowires have been mass manufactured by Vapor-Liquid-Solid mechanism (VLS), involving silane as a source of silicon. McFarland et al. [6] used Si nanowires as channels in Field Effect Transistors (FETs) to combat the size limitation encountered by the CMOS industry. In addition, sensitive biosensors were developed [7] by detecting the voltage modulation on the silicon nanowires before and after immobilization of biomolecules. Some of the other reported applications of Si nanowires include (a) anode material lithium ion batteries, (b) field emitters, (c) thermoelectric materials and currently in (d) photovoltaic applications.

Silicon is an attractive anode material for lithium batteries because it has a low discharge potential and the highest known theoretical charge capacity. However, bulk silicon anodes have limitations as silicon’s volume changes by 400% upon insertion and extraction of lithium, which results in pulverization and capacity fading. It has been shown that Si nanowire (Si NW) [8] battery electrodes circumvent these issues as they can accommodate large strain without pulverization, provide good electronic contact and conduction, and display short lithium insertion distances. Recent investigations indicate the use of Si nanowires in photovoltaics [9]. Upon fabricating p-n junctions conformally around the nanowire structure, the absorption of light can

be decoupled from minority carrier diffusion. Subsequently, minority carriers only have to diffuse tens to hundreds of nanometers to the charge-separating junction, rather than the tens to hundreds of microns typical of conventional solar cells. Silicon nanowires as alternate material for carrier transport nanowires offer several performance and manufacturing benefits that may impact future PV applications. The key to making silicon nanowire functional and leverage discernible enhancement from their bulk counterpart is to introduce defects both at atomic scale (boron, phosphorous...etc.) and at high concentrations (erbium) in the case of nanophotonic applications. As far as nanowire growth is concerned, research investigations aim to develop low temperature growth methodologies and silane free synthesis of wires.

#### **1.2.3.2 ZnO Nanowire**

An important class of functional nanomaterials arises from zinc oxide (ZnO) based nanostructures. Due to its wide band-gap (3.37 eV), near band emission, transparent conductivity, high exciton binding energy, and high breakdown strength, ZnO has been a promising nanomaterial for various applications. The inherent structure and a careful selection of process variables have enabled the nucleation of ZnO nanostructures with semiconducting, insulating and piezoelectric properties. Some of the potential applications [10] include:

Gas sensing is one application of ZnO nanostructures. ZnO is candidate material for gas sensing applications. ZnO shows oxygen deficiencies and surface defects in addition to high surface to volume ratio. Exposure to external ambient to ZnO nanorods induces a significant change in its conductivity/resistivity – high selectivity and sensitivity.

Optical emission by ZnO nanostructures is conducted. Zinc oxide is a very good light emitter. Electrically driven ZnO nanowire serves as high efficiency nanoscale light sources for optical data storage, imaging, and biological and chemical sensing.

Energy harvesting is another use of ZnO nanowires. Recently, ZnO nanowires have been used for energy harvesting applications. Piezoelectric ZnO NWs [11] have been used to convert nanoscale mechanical energy into electrical energy. In this investigation, the aligned NWs are deflected with a conductive atomic force microscope tip in contact mode. The coupling of piezoelectric and semiconducting properties in ZnO creates a strain field and charge separation across the NW as a result of its bending. The rectifying characteristic of the Schottky barrier formed between the metal tip and the NW leads to electrical current generation. The efficiency of the NW based piezoelectric power generator was estimated to be 17 to 30%. This approach has the potential of converting mechanical, vibrational, and/or hydraulic energy into electricity for powering nanodevices.

ZnO nanostructures are used to make Chemical/Biological sensors. The piezoelectric property of ZnO nanowires has also been exploited for chemical and biological sensing. The transduction mechanism to detect the desired chemical/biological species originates from compensation of the polarization-induced bound surface charge by interaction with polar molecules in the analyte. Also, the high aspect ratio and high isoelectric point of ZnO nanowires lends for efficient immobilization of high concentration of acidic enzymes and the mediating effect by the redox reactions.

The traditional challenge in growing aligned ZnO nanowires is the substrate compatibility due to lattice mismatch between ZnO and substrate. For example, ZnO

nanowires have a tendency to vertically align themselves on sapphire substrates where as in Si, process optimization is required.

### **1.2.3.3 Silica Nanowire**

Silica is one of the omnipresent elements existing in nature, primarily in the form of sand. It is a common constituent of glass and its derivative, like quartz. Undoubtedly, Silicon-di-oxide or silica has been the unsung hero of the semiconductor industry donning the role of an insulator. Bulk silica has been used in a plethora of applications such as (a) an insulating medium in CMOS circuits, (b) a barrier to prevent interfacial reactions in high temperature processing, (c) dielectric matrices/medium for synthesis of new materials as well as plasmonic applications, (c) masking material for high energy processes while offering a chemically compatible surface for etching applications and (d) a cell culture medium and biocompatible surface for developing in-vitro and in-vivo biosensors.

The aforementioned properties are enhanced multi-fold due to the high aspect ratio of the nanostructures and quantum confinement effects. Silica nanostructures have been manufactured in a variety of distinct topological forms (e.g. nanopores, nanospheres, nanowires, nanotubes, nanosprings etc....) giving rise to applications in optics, biosensing/clinical diagnostics, and catalysis and developing composites.

In general, silica nanostructures are known to possess characteristic structural properties (e.g., two-membered silicon dioxide rings [12], non-bridging oxygen (NBO) defects [13]) quite unlike those of the bulk, which is often reflected in their physical/chemical properties. Recently, for example, silica nanowires and nanotubes have been shown to be intense blue/visible light emitters [14], which have been linked to structurally non-stoichiometric defect centers. Recently, Mazur's group [15] fabricated long freestanding silica nanowires using a 'Taper Drawing' process with

diameters down to 50 nm that show atomic-level surface smoothness and excellent diameter uniformity. The length of the wires was estimated to be in tens of millimeters, giving them an aspect ratio larger than 50,000. It was shown that light can be launched along these wires by optical evanescent coupling. The wires enable single-mode operation and have very low optical losses within the visible to near-infrared spectral range. Also, mechanical tests show that the wires have tensile strength in excess of 5 GPa. The wires were also resilient and flexible, easily bending into microscopic loops. In contrast, silica nanotubes (SNTs) have proven to be a multifunctional nanostructure for biomedical applications [16] such as drug delivery and bioseparation. In a recent article, synthesis of well-controlled shape-coded SNTs and their application to biosensing as a new dispersible nanoarray system have been described. It is mentioned that the shape coded SNTs can be easily identified by their different shapes (codes) using a conventional optical microscope. Because of the low density and high surface area of the hollow tubular structure compared to those of the spherical and rod structures, SNTs can be suspended and are stable in solution.

#### **1.2.3.4 III-IV Semiconducting Nanowire**

III-IV compound semiconductor nanowires form an important sub-set functional nanostructure for optoelectronic applications, due to the direct bandgap and high carrier mobility of these materials. Various nanowire-based devices, including lasers and photodetectors, have already been demonstrated [17, 18]. Compound semiconductor nanowires like GaAs, InAs and InP have been investigated. It has been reported that homogenous InAs nanowires [19] show a low resistance at room temperature as well as at liquid helium temperature. A positive gate-voltage increases the conductance of a wire significantly and is found to be very sensitive to the diameter of the nanowires. Alternatively, InP nanowires serve as electron super

highways that carry electrons kicked loose by photons of light directly to the device's electron-attracting electrode and this scenario could boost thin-film solar cell efficiency as recently reported [20].

The growth of these nanowires is often carried out in MOCVD (Metal Organic Chemical Vapor deposition) with poisonous gases. However, the nanowire growth is limited to certain substrates which offer lattice matching to stress free nucleation of wires.

### **1.3 Nanowire-Growth Process**

During the last decade, one-dimensional nanostructures have been extensively investigated. Most of the studies have focused on the synthesis and fabrication of the nanostructures. Typically, two categories of synthesis and fabrication techniques are used. One is the so called "bottom-up" techniques using vapor phase deposition, chemical synthesis, self-assembly and location manipulations. The other is the "top-down" approach utilizing the lithography and precision engineered tools like cutting, etching, grinding etc. to fabricate nanoscale objects out of bulk materials. In the bottom-up category, several approaches have been well-established, which include an extensively explored vapor phase deposition method, including chemical vapor deposition (CVD) and physical vapor deposition (PVD), and liquid phase deposition (solution synthesis approach).

#### **1.3.1 Physical Vapor Deposition Method**

The traditional physical vapor deposition method is dedicated to the thin film and coating technology, which generally relies on the physical vaporization and condensation processes of materials. Based on the source of energy, five typical methods have been developed. The first one is the "thermal evaporation" process, which generally uses a resistor heater in a furnace to heat and facilitate the

vaporization of source materials and the nanostructure deposition process. This method has been fully developed as one of the most versatile methods for 1D nanostructure fabrication. The second type of PVD is the Electron-beam PVD, which has been extensively used for fabrications of ceramic thin film and coatings, but so far no reports have been found for application in 1D nanostructure synthesis. The third type of method is called “sputtering processes”. Sputtering is the removal of surface atoms due to bombardment from a flux of impinging energetic particles. The consequences of the interaction between an incident particle and a solid surface are mostly dictated by the kinetic energy of the projectile particle, although its internal energy may also play a significant role. Surface diffusion is usually used for explanation of the nanoscale islands or rods growth during the sputtering process. Cathodic arc discharge is another important physical vapor deposition method. It is famous for synthesis of the first batch of carbon nanotubes in 1993. It has been very popular as a method for fabrication of carbon related nanostructures, but there are very few applications in growth of oxide nanostructures. Pulse laser deposition (PLD) is a method for creation of nanostructures developed in the seminal work on  $\text{YBa}_2\text{Cu}_3\text{O}_{7-x}$  thin film growth by Venkatesan and co-workers in 1987 [21]. In the process, the source material is rapidly evaporated from a bulk target in a vacuum chamber by focusing a high power laser pulse on its surface. A large number of material types have been deposited as thin films using PLD. For some complex and high  $T_m$  (melting point) compounds, there is no doubt that using the PLD could be simpler and easier to receive a better quality of nanostructures. PLD has been used for synthesis of 1D nanostructure since early 90s in the last century. It has been successfully used in carbon nanotube synthesis with high yield instead of using cathode arc discharge, despite of a large amount of impurity. In the past decade, using

PLD method, a variety of 1D complex compound and core-shell structured nanostructure have been synthesized. Outside the auspices of high-performance semiconductor applications, PLD is as promising as any other technique for investigating new growth phenomena and systems, and it can offer some unique features.

### **1.3.2 Chemical Vapor Deposition**

Chemical vapor deposition (CVD) can be classified into six or more categories based on the difference of the vacuum control level, heating source and reactants gas types etc., as shown in Table I. Thermal CVD, LPCVD, LCVD, and MOCVD have been used to synthesize several types of nanowires. Using a similar set-up as the thermal evaporation method in PVD approach, thermal CVD just involves chemical reaction during the deposition process rather than a physical evaporation and deposition process. It has produced high quality carbon nanotube and nanowires including GaN [22, 23], GaAs etc. Like thermal evaporation in PVD, in thermal CVD, a solid source could be placed upstream. The solid is vaporized through heating, which is transported by a carrier gas that feeds the catalyst and source material for nanowire growth.

LPCVD is a technique for fabrication of a thermal oxide layer on semiconductor wafers in electronic industry. This approach uses a commercial oven or furnace as a main reaction chamber, which is generally composed of the reactant gas control and supply system and temperature/pressure control system. The pressure control is normally under 0.1 torr. Despite of an old technique for oxide film growth in electronic industry, recently the LPCVD has been a successful method for synthesis of various nanostructures such as carbon nanotube [24, 25], and Si nanowire [26-28], etc.

In Laser CVD, the CVD setup has been modified for laser ablation with controlled doses, leading to a control over nanowire lengths and diameters. Such a precision control made it possible to form superlattices [29] or core-shell [30] structures with doping. MBE has been used to grow 1D nanostructure of III-V group semiconductor compounds such as GaN [31], GaAs [32], InGaAs [25] and AlGaAs [33] etc. ALD seemingly has been used for fabrication of templates and ordered core-shell nanostructures [34-37] due to its precise control on atomic layer-by-layer deposition.

### **1.3.3 Solution-Based Chemical Synthesis Methods**

As a generic method for synthesis of nanostructures, chemical synthesis has been a powerful method for producing raw nanomaterials. Since the emergence of one-dimensional nanomaterials, solution based chemical synthesis methods have been extensively explored for fabrication of one-dimensional nanostructures. Many materials such as elemental noble metals Au, Pt, Ag, etc., tri- or multi-elemental compounds like Ba(Sr)TiO<sub>3</sub> [38,39], in nanowire-like shape have been successfully synthesized via solution based chemical synthesis methods, which cannot be easily fabricated by using vapor phase methods. The 1D nanostructures synthesized by chemical synthesis can be easily achieved in a large yield, but the large amount of impurities usually contained in the products always dramatically hinder their application, although complex post filtering and purification is useful for increasing its purity. From the cost point of view, a low-cost chemical synthesis with high yield undoubtedly is ideal for future commercialization of 1D nanostructure.

### **1.4 Nanowire Growth Kinetics**

The first most significant work on the mechanism of the unidirectional growth of semiconductor whiskers was published by Wagner and Ellis in 1964 [40]. They

produced Si whiskers on the Silicon substrate surface with Au as impurity by the Chemical Vapor Deposition growth technique and proposed the well-known Vapor-Liquid-Solid (VLS) mechanism. It is believed that whiskers grow due to the diffusion of vapor atoms on the alloy drop surface and the deposition of supersaturated liquid alloy on the surface under the drop [40-44]. In his published works, Givargizov discussed the four main steps during which nanowire was produced and he also drew some conclusions about the rate-determining step [42]. In 1973, Givargizov and Chernov put forward a theoretical model of whisker formation via VLS mechanism [41]. Since then, the VLS concept has been extended to include the nanometer-scale whiskers and widely used for explanation of Nanowire growth and the phenomenological Givargizov-Chernov model has been implemented [44-46]. The empirical formula from Givargizov and Chernov [41] for the whisker growth rate is shown by equation  $dL/dt = k_1(\Delta\mu/k_B T - k_2/D)^2$ . Here,  $\Delta\mu$  is the vapor supersaturation,  $T$  is the surface temperature,  $k_B$  is the Boltzmann constant,  $k_1$  is the unknown kinetic coefficient of growth for the solid-liquid interface in the step of the fourth in [42],  $k_2 = 2\alpha_{vs}\Omega/k_B T$ , in which  $\alpha_{vs}$  is the specific surface energy of the interface between the nanowire and the vapor around it and  $D$  represents the diameter. Givargizov and Chernov developed their equation based on the Gibbs-Thomson effect of elevation of chemical potential of cylindrically shaped crystal phase diameter  $D$ . It is reasonable that the  $-$ -dependent term appears in the equation. Kashchiev [47, 48] also proposed his own formula for the growth rate of nanowires with diameter  $D$ , but he did not take Gibbs-Thomson effect into account. He accounted for the transition from mono-nuclei to poly-nuclei mechanism of nucleation-mediated growth of nanowires. This effect is combined with the finite size of the growing surface on the substrate, which affects the number of droplets from which a nanowire is produced. In

mono-nuclei mechanism, the growth rate is proportional to  $D^2$  but in poly-nuclei mechanism it is independent of  $D$  so diameter  $D$  should be taken into account when transition from mono-nuclei to poly-nuclei mechanism of nucleation-mediated growth of nanowires is made. Kashchiev's formula reads  $dL/dt = a_1 D^2 / (1 + a_2 D^2)$ , where coefficients  $a_1$  and  $a_2$  depend on  $\Delta\mu$ , while their dependence on  $D$  can often be neglected. From the given expressions, it follows that both models predict the increasing length-diameter dependence, thicker Nanowires thus growing faster than the thinner ones. Such length-diameter dependence was obtained in many experiments on CVD growth of nanowires [41-43]. V.G. Dubrovskii and his co-workers [44-46] made great efforts in growth kinetics of GaAs nanoscale whiskers grown on the GaAs surface activated by Au and they proposed a new kinetic model describing the growth of nanoscale whiskers based on VLS mechanism in 2004. They aimed at the development of a kinetic model on Nanowire growth describing this process in a rather general form, containing the Givargizov-Chernov model as a particular case and accounted for both the Gibbs–Thomson effect and for the finite size of growing facet simultaneously [46]. Although it was reported later by Givargizov that diffusion in the liquid phase could not be the time-determining step [42], V. Ruth and J. P. Hirth introduced kinetics of diffusion-controlled whisker growth in 1964 [49]. In 2005, J. Kikka and co-workers [50] measured the growth rate of silicon nanowires that were grown at temperatures between 365 and 495°C via VLS mechanism and they studied the functions between growth rate and Temperature, time and diameter of nanowires. They finally got formula  $v_g(T, d) = \gamma^2(d)\alpha' \exp(-E_g / k_B T)$ , where  $E_g$  is the activation energy and  $\alpha'$  is a constant.

## **1.5 Challenges of Current Nanomanufacturing Process**

Nanomanufacturing represents the future of U.S. manufacturing. Nanostructured materials and processes have been predicted to increase their market impact to about \$340 billion per year in the next 10 years [51]. It has also been predicted that within the next 10 years, at least half of the newly designed advanced materials and manufacturing processes will be built at the nanoscale [52]. In the past decade, tremendous efforts have been devoted to basic nanoscience discovery, novel process development and concept proof of nano devices. Yet much less research activities have been undertaken in nanomanufacturing to duplicate the success of transforming quality and productivity performance of traditional manufacturing. The high cost of processing has been a major barrier to transferring the fast-developing nanotechnology from laboratories to industry applications [53]. The process yield of current nanodevices is typically 10% or less [54, 55]. The main challenge here is to improve process repeatability; therefore, there is an imperative need for process improvement methodologies for nanomanufacturing.

Understanding the first principles of nanostructure synthesis is certainly critical to improving process yield. Yet the physical laws are not completely understood at nanoscale. Current growth kinetics models involve a large number of constants to be estimated at a high level of accuracy. These models provide understanding of growth behavior at coarse scale, lack of description of local variability cross different sites on the substrate.

In traditional manufacturing, statistical quality control and engineering-driven statistical analysis of manufacturing process have achieved great success in yield and productivity improvement. Yet the scale effects bring new challenges on quality control in nanomanufacturing. First, manufacturing of quality-engineered

nanostuctures demands on prediction, monitoring and control of process variations at multiple scales. Second, nanostructure growth kinetics discovered in nanophysics provides valuable insights for process improvement. However, deterministic kinetics models fail to address process uncertainties. Third, there is a lack of in situ observation of most properties at the nanoscale during processing. The offline SEM (scanning electron microscope) or TEM (transmission electron microscopy) inspection is time-consuming and costly. These challenges call for systematic methodology to model and control nanomanufacturing processes.

Efforts have been undertaken to develop robust design methods to synthesize desired nanostructures [58] and to study the reliability of nanoelectronics [59-61]. The work on nanomanufacturing process control has not been reported.

Another big challenge lies in the characterization technology for nanoscale. Nanometrology is the science of measurement at the nanoscale level and it has a crucial role in order to produce nanomaterials and devices with a high degree of accuracy and reliability. Current characterization techniques are slow in data acquisition, especially in 3D measurement. Researchers have been developing measurement methods such as photogrammetry [56] and 3D reconstruction [57].

## **1.6 Research Objectives**

Huang (2009) [62] developed a nanowire growth process model at a fine scale for prediction. His model consists of two major components: nanowire morphology and local variability. The morphology component represents the overall trend characterized by growth kinetics. The area-specific variability, also named morphology variation, is less understood in nanophysics duo to complex interactions among neighboring nanowires. This thesis will mainly focus on nanostructure morphology variation modeling over different regions on the same substrate and

parameters estimation for the model by specifying the interactions among nanowires in the same system of sites.

## **1.7 Thesis Structure**

In this thesis, the first chapter, as stated above, is the introduction part, which shows the broad background of the research work.

The second chapter will describe the experiment and characterization methods. A measurement method will be proposed to obtain the length information from 2-dimensional SEM images. Two sets of the data on ZnO nanowire lengths has been collected.

The nanostructure morphology variation model will be built in Chapter 3 using Gaussian Markov random fields (GMRFs). Several numerical examples will be conducted according to the types of increment, which reflects the neighborhood structures in a GMRF.

The parameters in the model stated in the third chapter will be estimated in the fourth chapter by maximum likelihood estimation. Before the estimation, simulation studies are conducted to validate the model estimation method. The method then will be applied to the two sets of real data.

The last chapter will be the conclusion of this research work.

## **1.8 Summary**

This chapter first introduces nanotechnology and nanowire, which provides the board background of this research work. The growth process and the growth kinetics are then presented in details due to their importance in the research work. The research objective and the structure of the thesis are stated in the end.

## Chapter 2

### Experimental Methods and Characterization Techniques

Over the past decades, research into ZnO nanostructures has been one of the most attractive topics in physics, chemistry and materials science due to their significance in both fundamental and technological fields. In this chapter, we grow ZnO nanowires by chemical vapor deposition process and characterize ZnO nanowires from scanning electron microscopy (SEM) images.

#### 2.1 Introduction to Experiment System

The steps for ZnO nanowire synthesis in the experiment are briefly expressed by Fig.2:

1. Clean both the outer and the inner circular tubes and the substrate. This step is important because an airtight space to grow ZnO nanowires is necessary. If the outer circular tube is contaminated, it is very likely that the system leaks gas. When cleaning the substrate, use methanol instead of water.

2. Put 500 milligram ZnO powder and 500 milligram graphite in a slot container. In the replicates of the experiment, the mass and the ratio will remain the same. Put the gold deposited substrate in another slot container.

3. Put both of the containers into the inner circular tube and the ZnO powder is in front of the substrate. Notice that the thermocouple should be in the middle of the powder for the accuracy of the temperature detection.

4. Close the vent valve, switch on the mechanical pump, connect the vacuum gauge and then open the vacuum valve slowly. After about 15 minutes, the pressure in the gauge should be around 30 mtorr or at least less than 100 mtorr.

5. Open the hydrogen & Argon valve and then open the Hydrogen & Argon cylinders (Hydrogen should not be less than 200kPa or may be more, Argon is about 40psi). Switch on the mass flow controller. Channel 3 is for Argon and channel 4 is for hydrogen. Set up the gas flow rate of Argon and hydrogen. Pressure in the gauge increases and will be stable around 500 mtorr.

6. Turn on the digital temperature gauge, set the temperature rate at 10°C/min (Press the right button and hold for 3 seconds until “ctrl” appears on the top. Then press the “up” or “down” buttons until the “R.S” appears at the bottom. Press the right button to go back to the temperature display). Set the final temperature.

7. When the temperature reaches the final temperature, keep it at this high temperature for 30 minutes. Close the hydrogen valve, set the final temperature to room temperature (25°C) and close argon valve when the temperature reached 250°C.

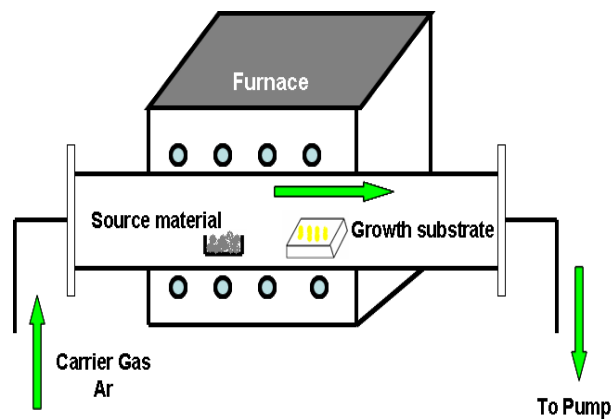


**Fig.2 A Diagram for ZnO Nanowires Synthesis**

## **2.2 Characterization Techniques**

The main technique used to observe and characterize ZnO is scanning electron microscopy (SEM). But the SEM images are in fact purely two-dimensional as the electron beam is scanned over the specimen surface. No height information can be

extracted directly from the images. The length of the nanowire is computed from two images obtained by observing the sample from two different angles/directions. The measurement method will be described in this section.

### 2.2.1 Scanning Electron Microscopy

An electron microscope is a type of microscope that uses electrons to illuminate the sample. Electron microscopes have much greater resolving power and can obtain higher magnifications than a light microscope. They can magnify specimens up to 2 million times, while the best light microscopes are limited to magnifications of 2000 times. Such a multi-fold enhancement in the resolution is due to the smaller wavelength of the electrons. For example, the wavelength of an electron induced by a 10 kV machine would be around 0.0123 nm whereas the visible wavelength of light ranges from 400-700 nm. Before proceeding in detail, the interaction of electrons with the surface of the sample needs to be understood.

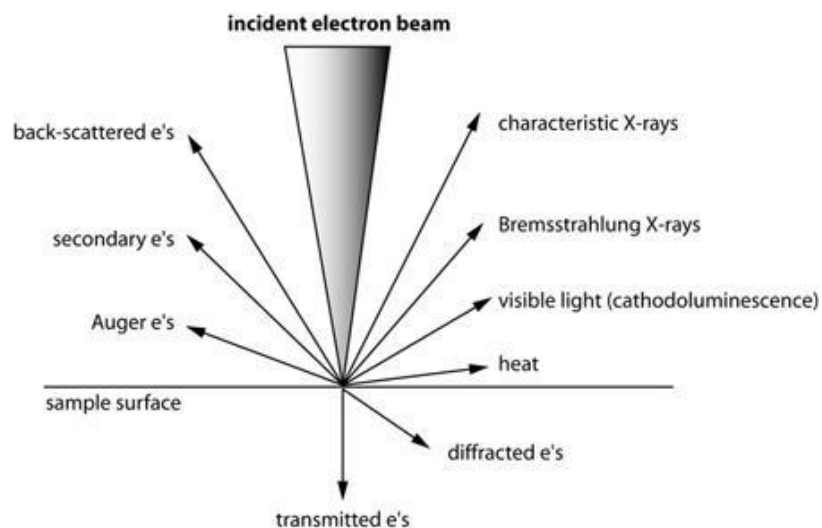


**Fig.3 Interactions of Electrons with the Sample**

[Courtesy: Geochemical Instrumentation and Analysis, Science Education  
Research Center, Carleton College]

When electrons bombard onto a surface, a number of interactions (Fig.3) arise with the atoms of the target sample. Accelerated electrons can either: (a) pass through the sample without interaction; (b) undergo elastic scattering or (c) undergo inelastic scattering. The scattering events result in unique signatures that can be used for imaging and quantitative information about the sample.

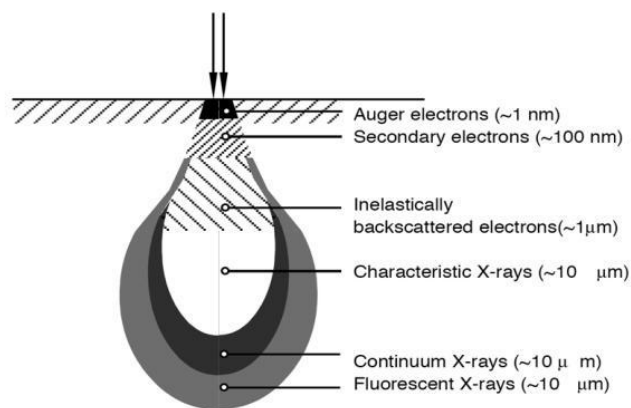


**Fig.4 Electron Interactions with Specimen-Scattering Events**

[Courtesy: Geochemical Instrumentation and Analysis, Science Education Research Center, Carleton College]

Typical signals include secondary electrons (SE), back scattered electrons (BSE), visible light, Auger electrons and characteristic X-rays arising from different depths in the sample, as shown on Fig.4. Secondary emission is produced by inelastic interactions of high energy electrons with valence electrons of atoms in the specimen. After undergoing additional scattering events while traveling through the specimen, some of these ejected electrons emerge from the surface of the specimen. The secondary electrons emerge with energies less than 50 eV. Further, larger atoms (with a greater atomic number, Z) have a higher probability of producing an elastic collision

because of their greater cross-sectional area. Consequently, the number of backscattered electrons (from a higher depth) reaching the detector is proportional to the mean atomic number of the sample. Thus, a "brighter" BSE intensity correlates with greater average Z in the sample, and "dark" areas have lower average Z. BSE images are very helpful for obtaining high-resolution compositional maps of a sample, thus enabling the differentiation of heavy and light elements/compounds and the metal/dielectric nature of the sample. The solid state detectors for collecting the secondary and back scattered electrons are placed on the side and in line with the electron gun respectively. Along with BSE image, the elemental and chemical composition is verified using energy dispersive spectroscopy.

### 2.2.2 Nanowire Length Measurement Development

The SEM images are in fact purely two-dimensional as the electron beam is scanned over the specimen surface. No height information can be extracted directly from the images. Fig.5 is a SEM image of ZnO nanowires; the length shown in the picture is not the true length of the nanowire but the top view of the true length.

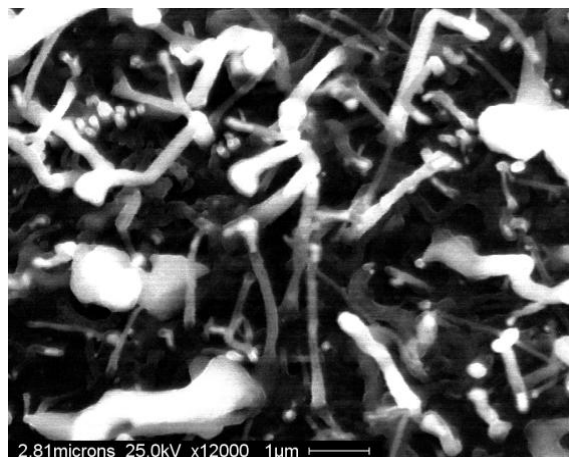


**Fig.5 SEM Image at the Magnification of 12K**

Based on the principles of photogrammetry [56], a general simplified measurement method for nanowire length is developed. The nanowires are observed

from two different angles/directions using scanning electron microscopy. By the following computation method, the height information can be extracted from the images.

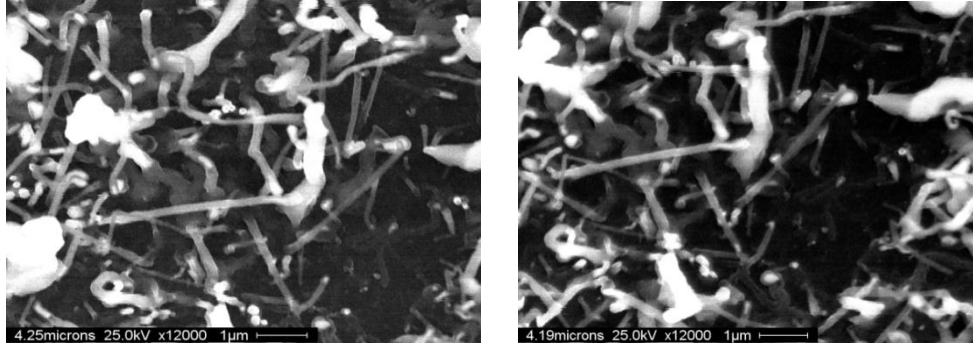


**Fig.6 ZnO Nanowires of the Same Region Observed from Different Angles**

The two SEM images of the same set of nanowires are obtained from two different angles, as shown by Fig.6. Shown on the CAD figure (Fig.7),  $L_1$  is the length of one nanowire observed at a certain angle and  $L_2$  is the length of the same nanowire observed after the rotation axis is tilted by an angle of 10 degree.

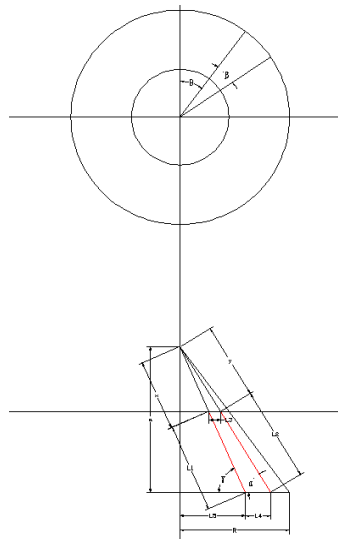


**Fig.7 The Position Change of the Same Nanowire after the Rotation**

From Fig.7,  $L_1$  and  $L_2$  can be obtained directly from the SEM images, and  $L_4$  is the distance at which the sample is moved to observe the same nanowire and thus  $L_4$  can be easily calculated by subtraction. The two angles  $\alpha$  and  $\gamma$  are the angles in between the horizontal line and the nanowire before and after the sample is tilted at an angle of 10 degrees.  $L_3$  can be computed by the equation (2.1).

$$L_3 = L_4 - (L_2 \cos \alpha - L_1 \cos \gamma) \quad (2.1)$$

When  $L_1, L_2, L_3, L_4$  are obtained, the extended part of the line  $x$  and  $y$  can be calculated by equations (2.2) and (2.3)

$$x = L_3 L_2 / (L_4 - L_3) \quad (2.2)$$

$$y = L_3 L_1 / (L_4 - L_3) \quad (2.3)$$

The length of  $a$  is the left view of the whole length of the nanowire, the equation (3.4) for computation of the left view is

$$a = (L_2 + x) \sin \alpha \quad (2.4)$$

$L_5$  is the top view of horizontal distance from the first position of the nanowire to the rotation axis;  $L_5 + L_4$  is the top view of horizontal distance from the second position of the nanowire to the rotation axis. The equation for  $L_5$  is

$$L_5 = \sqrt{(L_1 + y)^2 - a^2} \quad (2.5)$$

To get the value of  $R$ , which is the top view of the distance between the rotation axis and the imagined nanowire when it is on the substrate, and  $\theta$  which is the left view of the angle in between the rotation axis and the first position of the nanowire, we will have the nonlinear equations set,

$$\begin{aligned} R \sin \theta - L_5 &= 0 \\ R \sin(\theta + \beta) - (L_5 + L_4) &= 0 \end{aligned} \quad (2.6)$$

For the nonlinear equations set, the optimal solution of the equation (2.7) can be the right  $R$  and  $\theta$ .

$$|R \sin \theta - L_5| + |R \sin(\theta + \beta) - (L_5 + L_4)| = 0 \quad (2.7)$$

When the optimal solution is obtained, the length of the nanowire could be calculated by the equation (2.8).

$$L = \sqrt{R^2 + a^2} (L_4 - L_3) / L_4 \quad (2.8)$$

Note that two assumptions are taken in the computation method. The first assumption is that the electron beams are perpendicular to the surface of the substrate. In fact, the electrons are from a starting point; however, the assumption is acceptable because the distance from the starting point to the substrate surface is very long. The second assumption is that the nanowire being observed and the rotation axis are in the same plane.

### 2.2.3 Results and Data Tables

By the above measurement method, the length of nanowires can be obtained. The data in this research are spatial data, so the locations of the data are critical in data collections. Fig.8 shows the two sets of nanowires obtained from the scanning electron microscopy.

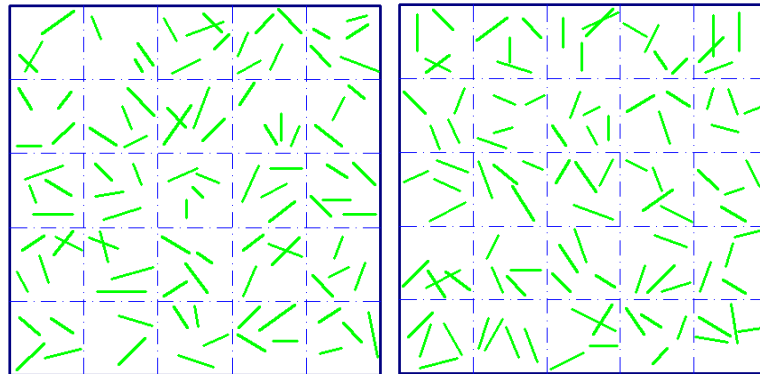


**Fig.8 The Two Sets of the Observed Nanowires**

By the measurement method developed above, the length of the observed nanowires can be obtained.

Data Table 1 (Data Set 1) shows the lengths of the nanowires from the first observation. The data are filled into a regular lattice for the convenience of modeling.

**Table 1: Data of Lengths for the First Set of Nanowires**

|      |      |      |      |      |      |      |      |      |      |
|------|------|------|------|------|------|------|------|------|------|
| 5.01 | 2.27 | 3.07 | 2.58 | 3.24 | 3.61 | 3.43 | 2.41 | 1.97 | 3.52 |
| 4.32 | 3.65 | 1.71 | 1.54 | 3.17 | 2.49 | 2.38 | 3.34 | 2.91 | 3.26 |
| 1.88 | 2.46 | 2.63 | 2.92 | 2.66 | 3.79 | 1.94 | 3.15 | 2.79 | 4.48 |
| 3.91 | 3.25 | 1.89 | 2.51 | 4.27 | 3.74 | 2.89 | 2.65 | 3.03 | 1.87 |
| 4.56 | 2.32 | 2.18 | 2.27 | 2.14 | 4.19 | 4.77 | 3.04 | 2.65 | 3.07 |
| 2.73 | 2.33 | 3.33 | 2.59 | 4.82 | 2.48 | 3.67 | 4.57 | 4.46 | 4.65 |
| 2.57 | 2.53 | 2.36 | 2.68 | 3.58 | 2.60 | 3.92 | 3.13 | 3.69 | 3.97 |
| 2.96 | 2.31 | 3.51 | 2.57 | 2.56 | 3.62 | 2.76 | 2.75 | 2.83 | 3.31 |
| 2.91 | 3.54 | 2.85 | 2.79 | 1.80 | 2.08 | 2.91 | 2.99 | 2.58 | 2.38 |
| 2.88 | 3.26 | 2.99 | 2.75 | 1.82 | 2.54 | 3.31 | 2.13 | 3.32 | 2.39 |

Fig.9 shows the morphology variation from the above data in lattice which is collected in one region on the substrate.

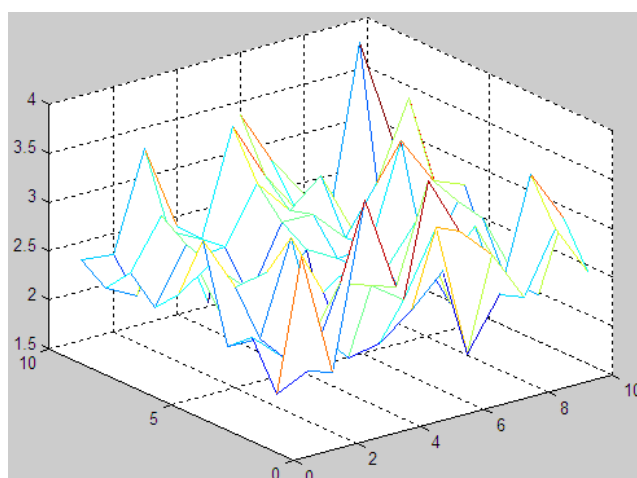


**Fig.9 Morphology Variation from the Data Set 1**

Data Table 2 (Data Set 2) shows the lengths of the nanowires from the second observation. The size of this set of data is exactly the same as the first set and it is used for validation.

**Table 2: Data of Lengths for the Second Set of Nanowires**

|      |      |      |      |      |      |      |      |      |      |
|------|------|------|------|------|------|------|------|------|------|
| 3.38 | 2.11 | 3.79 | 2.81 | 3.81 | 3.21 | 2.88 | 2.36 | 2.97 | 2.45 |
| 1.86 | 2.01 | 2.83 | 2.71 | 2.48 | 3.13 | 1.75 | 2.27 | 3.41 | 2.89 |
| 2.33 | 2.03 | 2.24 | 1.86 | 1.92 | 2.17 | 2.48 | 2.86 | 2.23 | 1.98 |
| 2.13 | 2.12 | 3.06 | 2.42 | 2.63 | 2.49 | 2.91 | 1.95 | 2.73 | 2.07 |
| 3.09 | 2.53 | 2.59 | 2.01 | 1.67 | 2.35 | 1.75 | 2.26 | 2.79 | 2.10 |
| 2.42 | 2.65 | 2.34 | 2.18 | 2.54 | 2.36 | 2.39 | 3.38 | 2.89 | 2.76 |
| 2.18 | 2.74 | 1.97 | 2.03 | 2.70 | 2.69 | 2.36 | 2.83 | 3.62 | 2.44 |
| 2.42 | 2.91 | 2.39 | 2.42 | 2.98 | 2.61 | 2.88 | 2.23 | 2.05 | 1.76 |
| 2.15 | 1.98 | 2.55 | 2.38 | 3.45 | 2.86 | 2.43 | 2.19 | 3.96 | 2.89 |
| 2.33 | 2.29 | 3.29 | 2.41 | 1.54 | 3.36 | 2.82 | 2.38 | 2.31 | 2.52 |

Fig.10 shows the morphology variation from the above data in lattice which is collected in a different region on the same substrate.

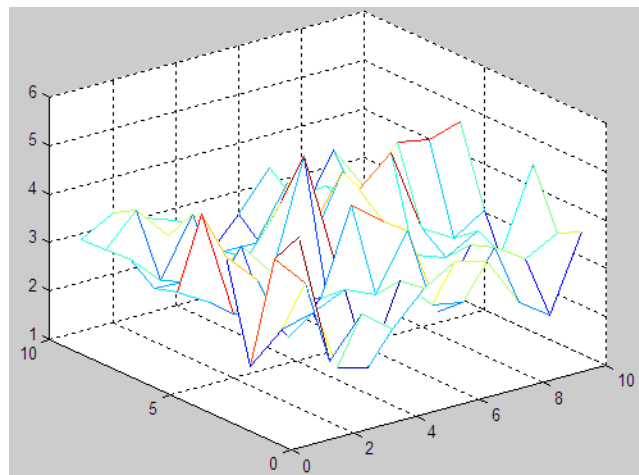


**Fig.10 Morphology Variation from the Data Set 2**

### **2.3 Summary**

In this chapter, the experiment is described followed by the introduction of characterization techniques. The most popular and effective technique currently is scanning electron microscopy. Through a systematic investigation of the three-dimensional scanning techniques, a simplified measurement method for ZnO nanowire length from two SEM images obtained from two different angles has been developed. The measurement method follows the principles of Photogrammetry and the two SEM images are achieved by tilting the rotational axis at a given degree of angle. The computation code is developed due to the large amount of data and the difficulty to obtain the solutions for nonlinear equations set. Two sets of data, each of which is of size 10 by 10, are finally collected for the use of parameter estimation in the following chapters.

## Chapter 3

### Nanostructure Morphology Variation Modeling

Huang (2009) [62] pointed out that nanostructure growth is a dynamic process which is to be characterized by a space-time random field model. His model consists of two major components: nanowire morphology and local variability. The morphology component represents the overall trend characterized by growth kinetics. The area-specific variability, namely morphology variation, is less understood in nanophysics due to complex interactions among neighboring nanowires. In this chapter, the nanostructure growth model will be introduced first and then we will focus on nanostructure morphology variation modeling on both infinite lattice and finite lattice by specifying the interactions among nanowires in some neighborhood structures.

#### 3.1 Space-Time Random Field Model of Nanostructure Morphology

Let  $X$  represent the quality features of nanowires on a substrate. At a certain scale and time  $t$ , the observed feature at site  $s_i$  of the substrate is denoted as  $X(s_i, t)$ ,  $s_i \in R^p$ ,  $p \in \{1, 2, 3\}$ ,  $i = 1, 2, 3, \dots, n$ . For simplicity of presentation we hereafter only show the case with  $p = 1$ . All the features at sites  $s = (s_1, s_2, \dots, s_n)^T$  are represented as  $\mathbf{X}(s, t)$ :

$$\mathbf{X}(s, t) = [X(s_1, t), X(s_2, t), \dots, X(s_3, t), \dots, X(s_n, t)]^T \quad (3.1)$$

which is a space-time random field on lattice  $s$ .

In the space-time random field model, Huang [62] decomposed the nanostructure random field  $X(s, t)$  into morphology or profile  $\boldsymbol{\eta}_{k-1}(s, t)$ , local variation  $\boldsymbol{\varphi}(s)$  and noise  $\varepsilon$ ,

$$X(s, t) = \boldsymbol{\eta}_{k-1}(s, t) + \boldsymbol{\varphi}(s) + \varepsilon \quad (3.2)$$

where  $\boldsymbol{\eta}_{k-1}(s, t)$  could be a plane or a surface with relative complex profile evolving over the growth process.  $\boldsymbol{\varphi}(s)$  represents the local fluctuation riding on the morphology. A Gaussian Markov random field (GMRF) is suggested to be applied to model  $\boldsymbol{\varphi}(s)$ , which will be the main task in this chapter.

The rationale of the morphology-local decomposition is as follows. Currently there is better understanding of global behaviors of the growth kinetics but limited physical knowledge is available for area-specific variability. The decomposition therefore aims at engaging growth kinetics through  $\boldsymbol{\eta}_{k-1}(s, t)$  and morphology variation modeling through  $\boldsymbol{\varphi}(s)$ . Due to the lack of physical studies, we only consider the case that local variability at site  $s_i$  is mainly determined by its interaction with neighbors and remains stable over time.

### 3.2 Motivation of Modeling via Gaussian Markov Random Fields

It is suggested that a GMRF be applied to model the local variability in nanostructure growth. Actually an alternative method of modeling the nanostructure is to use the kriging model in spatial statistics [63, 64].  $X(s_i, t)$  would be expressed as  $X(s_i, t) = \mu(s_i, t) + Z(s_i)$ , where  $\mu(s_i, t)$  is a mean function and  $Z(s_i)$  weak stationary Gaussian field (see a kriging example in computer experiments [65]). The kriging model also captures the trend and local variability, and there is a connection between Gaussian random field and Gaussian Markov random field [66]. We prefer a Markovian property for the local variability component and a noise term  $\varepsilon$  in

equation (3.2) for two reasons [62]:

- ◆ First, we intend to separate the modeling error and noise (see a general discussion in [21]). The modeling error in equation (3.2) dominates in  $\varphi(s)$  due to the lack of understanding at fine scales. However, molecular dynamics simulation [67] often use, e.g. the Lennard-Jones potential [68] to describe the interactions among nanowires or nanotubes. The separation offers the opportunity to adopt result in molecular dynamics to model the covariance structure in  $\varphi(s)$  at nanoscale in the future.
- ◆ Second, Gaussian Markov random field has shown the flexibility to specify the neighborhood structure on a lattice and to improve the efficiency in computation [66]. Material properties such as anisotropy are easier to be modeled. Although the advantages of this modeling treatment may not be fully demonstrated until the multiscale modeling and control methodologies are developed, it can be viewed as one viable strategy to model the nanostructure growth process with effective integration of nanophysics.

### 3.3 Modeling of Nanowire Morphology Variation

As defined in equation (3.2), the area-specific variability  $\varphi(s)$  represents local fluctuation riding on the morphology. In addition,  $\varphi(s)$  is expected to capture the dependence/interaction among neighboring sites. We adopt an intrinsic Gaussian Markov random field model with rank deficiency  $k$  in a line for local variability  $\varphi(s) = [\phi(s_1), \phi(s_2), \dots, \phi(s_i), \dots, \phi(s_{k-1})]^T$ . It has density function [66]

$$f[\varphi(s)] = (2\pi)^{\frac{n-k}{2}} |\mathbf{Q}|^{\frac{1}{2}} \exp\left[-\frac{1}{2} (\varphi(s) - \boldsymbol{\mu}^*)^T \mathbf{Q} (\varphi(s) - \boldsymbol{\mu}^*)\right] \quad (3.3)$$

where  $\mathbf{Q}$  is precision matrix with rank  $n - k$  and  $|\mathbf{Q}|^*$  denotes the generalized determinant.

The local variability  $\boldsymbol{\varphi}(s)$  specified by equation (3.3) will mainly be determined by the structure of the precision matrix. For an IGMRF of first order ( $k=1$ ), the conditional mean of  $\phi(s_i)$  is simply a weighted average of its neighbors, not involving an overall mean, i.e.,  $E[\phi(s_i) | \boldsymbol{\varphi}(s_{-i})] = -\frac{1}{Q_{ii}} \sum_{j:j \sim i} \phi(s_j)$  [66]. Notation  $j: j \sim i$  denotes the sites  $s_j$ 's that are the neighbors of  $s_i$ .

Let  $\boldsymbol{\varphi}(s)$  be modeled via a Gaussian Markov random field with precision matrix  $\boldsymbol{Q}$  and the overall mean of  $\boldsymbol{\varphi}(s)$  be  $\boldsymbol{\mu}$ , we have [66],

$$E(\phi(s_i) | \boldsymbol{\varphi}(s_{-i})) = \mu_i - \frac{1}{Q_{i,i}} \sum_{j:j \sim i} Q_{i,j} (\phi(s_j) - \mu_j) \quad (3.4)$$

$$\text{Corr}(\phi(s_i), \phi(s_j) | \boldsymbol{\varphi}(s_{-(i,j)})) = -\frac{Q_{i,j}}{\sqrt{Q_{i,i} Q_{j,j}}}, i \neq j \quad (3.5)$$

$$\text{Prec}(\phi(s_i) | \boldsymbol{\varphi}(s_{-i})) = Q_{i,i} \quad (3.6)$$

It is clear that to model nanostructure morphology variation, constructing the precision matrix  $\boldsymbol{Q}$  for a Gaussian Markov random field is critical. The process defined by equation (3.3) is called conditional autoregression Gaussian scheme [69], for which

$$E(\phi(s_i) | \boldsymbol{\varphi}(s_{-i})) = \mu_i + \sum \beta_{i,j} (\phi(s_j) - \mu_j) \quad (3.7)$$

It is worth indicating the distinction between this scheme and the process defined by simultaneous autoregressive scheme, typically

$$\phi(s_i) = \mu_i + \sum \beta_{i,j} (\phi(s_j) - \mu_j) + \varepsilon_i \quad (3.8)$$

where  $\varepsilon_1, \dots, \varepsilon_n$  are independent Gaussian variants, each with zero mean and variance  $\kappa^{-1}$ . In contrast to equation (3.3), the latter process has joint probability density function,

$$f[\boldsymbol{\varphi}(s)] = (2\pi)^{\frac{n-k}{2}} |\mathbf{Q}|^{-1} \exp\left[-\frac{1}{2}(\boldsymbol{\varphi}(s) - \boldsymbol{\mu}^*)^T \mathbf{Q} \boldsymbol{\varphi}(s) - \boldsymbol{\mu}^*\right] \quad (3.9)$$

where  $\mathbf{Q}$  is defined the same way as the  $\mathbf{Q}$  in the conditional autoregression Gaussian scheme, which will be constructed in the next section.

### 3.4 Construction of Precision Matrix of GMRFs

To construct the precision matrix for GMRFs, the most critical issue is to define the neighborhood structures which include two basic aspects: (i) labeled graph [66] and (ii) interactions among the nanostructures. Labeled graph determines the related neighbors and the interactions are the weights of the related neighbors.

#### 3.4.1 Precision Matrix for Infinite Lattice

To construct precision matrix of GMRFs on infinite lattices, both of the above two aspects in the neighborhood structures can be represented in conditional autoregression Gaussian scheme and the simultaneous autoregressive scheme.

##### 3.4.1.1 Conditional Autoregression Scheme

In the conditional autoregression Gaussian scheme (3.3),  $\mathbf{Q}$  is the  $n \times n$  matrix whose diagonal elements are unity and whose off-diagonal  $(i, j)$  element is  $-\beta_{i,j}$ . Clearly  $\mathbf{Q}$  is symmetric and is nonsingular [69].

For example, we have a conditional autoregression Gaussian scheme as follows,

$$E[\phi(s_{i,j}) | \boldsymbol{\varphi}(s_{-(i,j)})] = \mu_{i,j} + 0.25\phi(s_{i-1,j}) + 0.25\phi(s_{i+1,j}) + 0.25\phi(s_{i,j-1}) + 0.25\phi(s_{i,j+1}) \quad (3.10)$$

The precision matrix  $\mathbf{Q}$  for a 3 by 3 lattice would be,

$$\mathbf{Q} = \begin{pmatrix} 1 & -0.25 & 0 & -0.25 & 0 & 0 & 0 & 0 & 0 \\ -0.25 & 1 & -0.25 & 0 & -0.25 & 0 & 0 & 0 & 0 \\ 0 & -0.25 & 1 & 0 & 0 & -0.25 & 0 & 0 & 0 \\ -0.25 & 0 & 0 & 1 & -0.25 & 0 & -0.25 & 0 & 0 \\ 0 & -0.25 & 0 & -0.25 & 1 & -0.25 & 0 & -0.25 & 0 \\ 0 & 0 & -0.25 & 0 & -0.25 & 1 & 0 & 0 & -0.25 \\ 0 & 0 & 0 & -0.25 & 0 & 0 & 1 & -0.25 & 0 \\ 0 & 0 & 0 & 0 & -0.25 & 0 & -0.25 & 1 & -0.25 \\ 0 & 0 & 0 & 0 & 0 & -0.25 & 0 & -0.25 & 1 \end{pmatrix} \quad (3.11)$$

From Rue and Held [66], for a conditional autoregression scheme,

$$\phi(s_i | \mathbf{s}_{-i}) \sim N\left(\sum_{j:j \neq i} \beta_{i,j} \phi(s_j), \kappa^{-1}\right) \quad (3.12)$$

the precision matrix has elements

$$Q_{i,j} = \begin{cases} \kappa, & i = j \\ \kappa \beta_{i,j}, & i \neq j \end{cases} \quad (3.13)$$

It is assumed that the variance of  $\phi(s_i | \mathbf{s}_{-i})$  is a constant and thus the precision matrix from equation (3.13) for a 3 by 3 lattice is the multiplication of  $\kappa$  and equation (3.11).

### 3.4.1.2 Simultaneous Autoregressive Scheme

For the simultaneous autoregressive scheme (3.9), the precision matrix  $Q$  will be

$$Q = B^T B \quad (3.14)$$

$B$  is defined the same as  $Q$  in the conditional autoregression scheme, which is shown by Eq.(3.13).

For example, we have a simultaneous autoregressive scheme as follows,

$$\phi(s_{i,j}) = \mu_{i,j} + 0.25\phi(s_{i-1,j}) + 0.25\phi(s_{i+1,j}) + 0.25\phi(s_{i,j-1}) + 0.25\phi(s_{i,j+1}) + \varepsilon_{i,j} \quad (3.15)$$

The precision matrix  $Q$  for a 3 by 3 lattice will be

$$Q = \begin{pmatrix} 1.125 & -0.5 & 0.0625 & -0.5 & 0.125 & 0 & 0.0625 & 0 & 0 \\ -0.5 & 1.1875 & -0.5 & 0.125 & -0.5 & 0.125 & 0 & 0.0625 & 0 \\ 0.0625 & -0.5 & 1.125 & 0 & 0.125 & -0.5 & 0 & 0 & 0.0625 \\ -0.5 & 0.125 & 0 & 1.1875 & -0.5 & 0.0625 & -0.5 & 0.125 & 0 \\ 0.125 & -0.5 & 0.125 & -0.5 & 1.25 & -0.5 & 0.125 & -0.5 & 0.125 \\ 0 & 0.125 & -0.5 & 0.0625 & -0.5 & 1.1875 & 0 & 0.125 & -0.5 \\ 0.0625 & 0 & 0 & -0.5 & 0.125 & 0 & 1.125 & -0.5 & 0.0625 \\ 0 & 0.0625 & 0 & 0.125 & -0.5 & 0.125 & -0.5 & 1.1875 & -0.5 \\ 0 & 0 & 0.0625 & 0 & 0.125 & -0.5 & 0.0625 & -0.5 & 1.125 \end{pmatrix} \quad (3.16)$$

This  $Q$  is calculated by equation (3.14), in which  $B$  is the same as  $Q$  in equation (3.11).

### 3.4.2 Precision Matrix for Finite Lattice

The precision matrices defined above are for the infinite lattice and are definite. The case where  $\mathbf{Q}$  is symmetric and positive semidefinite is of particular interest. The class is known under the name intrinsic Gaussian Markov random fields. We construct precision matrix  $\mathbf{Q}$  of these random fields based on the concept of the  $k^{th}$  order increments, which are directly from the simultaneous autoregressive scheme.

Like the simultaneous autoregressive scheme, the increments also contain both aspects in the neighborhood structures. The  $k^{th}$  order increments define the related neighbors and the coefficients of the neighbors in the increments are the interactions, namely the weights of the related neighbors. For example, the second order forward increments in two directions,

$$(\Delta_{(1,0)} + \Delta_{(0,1)})^2 \phi(s_{i,j}) = 4\phi(s_{i,j}) - 4\phi(s_{i,j+1}) + \phi(s_{i,j+2}) - 4\phi(s_{i+1,j}) + 2\phi(s_{i+1,j+1}) + \phi(s_{i+2,j}) \sim N(0, \kappa^{-1})$$

Follow the computation method proposed by Rue and Held [62], to define the joint density of  $\boldsymbol{\varphi}$ :

$$\begin{aligned} \pi(\boldsymbol{\varphi}) &\propto \kappa^{(n_r * n_c - 2)/2} \exp\left(-\frac{1}{2} \sum_{i=1}^{n_r-2} \sum_{j=1}^{n_c-2} 4\phi(s_{i,j}) - 4\phi(s_{i,j+1}) + \phi(s_{i,j+2}) - 4\phi(s_{i+1,j}) + 2\phi(s_{i+1,j+1}) + \phi(s_{i+2,j})\right)^2 \\ &= \kappa^{(n_r * n_c - 2)/2} \exp\left(-\frac{1}{2} \boldsymbol{\varphi}^T \mathbf{Q} \boldsymbol{\varphi}\right) \end{aligned} \quad (3.17)$$

The precision matrix for a lattice with size of 3 by 3 shown by Fig.11 is

$$\mathbf{Q} = \kappa \begin{pmatrix} 16 & -16 & 4 & -16 & 8 & 0 & 4 & 0 & 0 \\ -16 & 16 & -4 & 16 & -8 & 0 & -4 & 0 & 0 \\ 4 & -4 & 1 & -4 & 2 & 0 & 1 & 0 & 0 \\ -16 & 16 & -4 & 16 & -8 & 0 & -4 & 0 & 0 \\ 8 & -8 & 2 & -8 & 4 & 0 & 2 & 0 & 0 \\ 0 & 0 & 0 & 0 & 0 & 0 & 0 & 0 & 0 \\ 4 & -4 & 1 & -4 & 2 & 0 & 1 & 0 & 0 \\ 0 & 0 & 0 & 0 & 0 & 0 & 0 & 0 & 0 \\ 0 & 0 & 0 & 0 & 0 & 0 & 0 & 0 & 0 \end{pmatrix} \quad (3.18)$$

The entries in precision matrix are the interactions of the corresponding combination of the sites. For example, the elements in the first row are the interactions of the combinations from  $\phi(s_{1,1})\phi(s_{1,1})$ ,  $\phi(s_{1,1})\phi(s_{1,2})$  to  $\phi(s_{1,1})\phi(s_{3,2})$ ,  $\phi(s_{1,1})\phi(s_{3,3})$  when we study the site of  $\phi(s_{1,1})$ . By the above precision matrix, the edge effects can be obviously interpreted. The interactions of the combinations which contain  $\phi(s_{3,3})$  are all zeroes because  $\phi(s_{3,3})$  is on the edge. When we take the forward increments for constructing precision matrix for GMRFs, only the interactions between  $\phi(s_{3,3})$  and the coming sites, like  $\phi(s_{3,4})$  and  $\phi(s_{4,3})$ , are not zeroes. By comparing equations (3.11), (3.16) with (3.18), we can figure out the differences between the precision matrices of GMRFs on infinite lattice and those on finite lattice. The precision matrices on infinite lattices are all non-singular; the precision matrices on finite lattices are singular and contain a large quantity of zero elements, which are called sparse matrices and will lead to efficiency in computation. The edge effect is quite significant when the lattice is large and it is the reason for the rank deficiency of the precision matrices for GMRFs.

We have the conclusions based on the above precision matrix,

$$16E(\phi(s_{1,1})) - 16\phi(s_{1,2}) + 4\phi(s_{1,3}) - 16\phi(s_{2,1}) + 8\phi(s_{2,2}) + 4\phi(s_{3,1}) = 0 \quad (3.19)$$

$$E(\phi(s_{1,1})) = \phi(s_{1,2}) - \frac{1}{4}\phi(s_{1,3}) + \phi(s_{2,1}) - \frac{1}{2}\phi(s_{2,2}) - \frac{1}{4}\phi(s_{3,1}) \quad (3.20)$$

|                 |                 |                 |
|-----------------|-----------------|-----------------|
| $\phi(s_{1,1})$ | $\phi(s_{1,2})$ | $\phi(s_{1,3})$ |
| $\phi(s_{2,1})$ | $\phi(s_{2,2})$ | $\phi(s_{2,3})$ |
| $\phi(s_{3,1})$ | $\phi(s_{3,2})$ | $\phi(s_{3,3})$ |

**Fig.11 A 3 by 3 Lattice of Local Variability**

Other examples of the increments are central increments (3.21) and the forward increments without diagonal terms (3.22).

$$(\Delta^2_{(1,0)} + \Delta^2_{(0,1)})\phi(s_{i-1,j-1}) = (\phi(s_{i+1,j}) + \phi(s_{i-1,j}) + \phi(s_{i,j+1}) + \phi(s_{i,j-1})) - 4\phi(s_{i,j}) \sim N(0, \kappa^{-1}) \quad (3.21)$$

$$(\Delta^2_{(1,0)} + \Delta^2_{(0,1)})\phi(s_{i,j}) = 2\phi(s_{i,j}) - 2\phi(s_{i,j+1}) + \phi(s_{i,j+2}) - 2\phi(s_{i+1,j}) + \phi(s_{i+2,j}) \sim N(0, \kappa^{-1}) \quad (3.22)$$

The fourth type of increments is from covariance functions and weights functions in Spatial Statistics [63]. We know for two nodes  $i$  and  $j$ , there would be a couple of covariance functions, such as:

$$\text{Exponential covariance function: } C(h) = \exp(-3h)$$

$$\text{Gaussian covariance function: } C(h) = \exp(-3h^2)$$

$$\text{Powered covariance function: } C(h) = \exp(-3h^\alpha), 0 < \alpha \leq 2$$

where  $h$  is Euclidean distance between two sites.

To define a proper neighborhood system, it is obvious that two sites should be neighbors when their covariance is large. In spatial statistics, we also know several types of weights functions, such as  $d^{-2}$ ,  $e^{-ad}$ ,  $e^{-ad^2}$  and  $w(d) = (e^{-d^2/\alpha})/(d^2 + \varepsilon)$ . Here, we choose exponential covariance function, the decision boundary is 0.001 and the weights function  $d^{-2}$  as an example.

Based on these ideas, we will have increments as follows:

$$\begin{aligned} (\Delta^2_{(1,0)} + \Delta^2_{(0,1)})\phi(s_{i-1,j-1}) &= \frac{1}{43}\phi(s_{i-2,j-1}) + \frac{5}{174}\phi(s_{i-2,j}) + \frac{1}{43}\phi(s_{i-2,j+1}) + \frac{1}{43}\phi(s_{i-1,j-2}) \\ &+ \frac{5}{86}\phi(s_{i-1,j-1}) + \frac{5}{43}\phi(s_{i-1,j}) + \frac{5}{86}\phi(s_{i-1,j+1}) + \frac{1}{43}\phi(s_{i-1,j+2}) + \frac{5}{174}\phi(s_{i,j-2}) + \frac{5}{43}\phi(s_{i,j-1}) \\ &- \phi(s_{i,j}) + \frac{5}{43}\phi(s_{i,j+1}) + \frac{5}{174}\phi(s_{i,j+2}) + \frac{1}{43}\phi(s_{i+1,j-2}) + \frac{5}{86}\phi(s_{i+1,j-1}) + \frac{5}{43}\phi(s_{i+1,j}) \\ &+ \frac{5}{86}\phi(s_{i+1,j+1}) + \frac{1}{43}\phi(s_{i+1,j+2}) + \frac{1}{43}\phi(s_{i+2,j-1}) + \frac{5}{174}\phi(s_{i+2,j}) + \frac{1}{43}\phi(s_{i+2,j+1}) \sim N(0, \kappa^{-1}) \end{aligned} \quad (3.23)$$

In conclusion of this section, the precision matrices are constructed from the conditional autoregression Gaussian scheme, the simultaneous autoregressive scheme and the increments. The intrinsic Gaussian Markov random field from the increments

plays a critical role in the model described in the first section of Chapter 3, because the intrinsic Gaussian Markov random field is invariant to the addition of polynomials, which is also mentioned in the paper by Huang [62]. When the precision is obtained, the morphology variation could be simulated from the model.

### 3.5 The Simulation of Morphology Variation by Improper GMRF

With the precision matrix obtained in the above section, we can simulate the morphology variation for improper GMRFs by the algorithm from Rue and Held [66]. We simulate the morphology variation for a lattice with 20 rows and 20 columns.

The simulation for the finite lattice from improper GMRF constructed based on the central increments is shown by Fig.12. The central increments are

$$(\Delta_{(1,0)}^2 + \Delta_{(0,1)}^2)\phi(s_{i-1,j-1}) = (\phi(s_{i+1,j}) + \phi(s_{i-1,j}) + \phi(s_{i,j+1}) + \phi(s_{i,j-1})) - 4\phi(s_{i,j}) \sim N(0, \kappa^{-1})$$

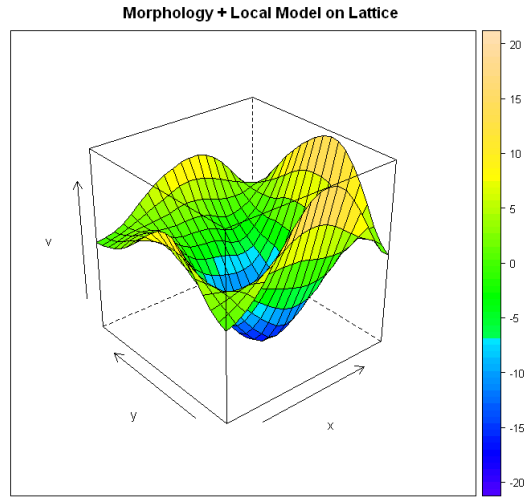


**Fig.12 Simulation for Central Increments**

The simulation for the finite lattice from improper GMRF constructed based on the forward increments is shown by Fig.13. The forward increments with interactions are

$$(\mathcal{A}_{(1,0)} + \mathcal{A}_{(0,1)})^2 \phi(s_{i,j}) = 4\phi(s_{i,j}) - 4\phi(s_{i,j+1}) + \phi(s_{i,j+2}) - 4\phi(s_{i+1,j}) + 2\phi(s_{i+1,j+1}) + \phi(s_{i+2,j}) \sim N(0, \kappa^{-1})$$

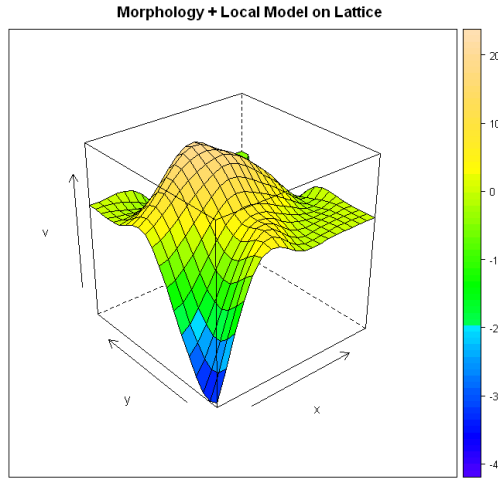


**Fig.13 Simulation for Forward Increments with Interactions**

The simulation for the finite lattice from improper GMRF constructed based on the forward increments without diagonal terms is shown by Fig.14. The forward increments without diagonal terms are

$$(\Delta^2_{(1,0)} + \Delta^2_{(0,1)})\phi(s_{i,j}) = 2\phi(s_{i,j}) - 2\phi(s_{i,j+1}) + \phi(s_{i,j+2}) - 2\phi(s_{i+1,j}) + \phi(s_{i+2,j}) \sim N(0, \kappa^{-1})$$

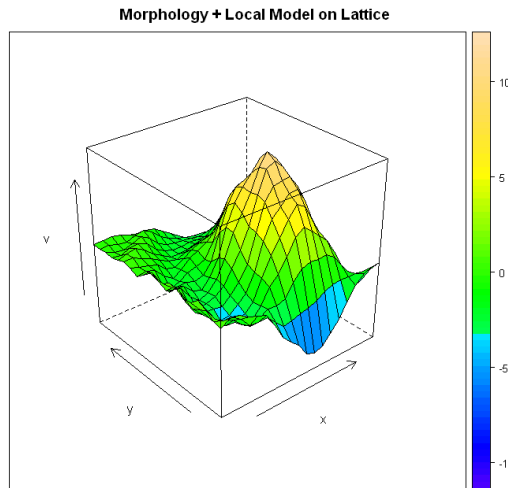


**Fig.14 Simulation for Forward Increments without Interactions**

The simulation for finite lattice from improper GMRF constructed based on the interactions in spatial statistics is shown by Fig.15. The increments are

$$\begin{aligned}
(\Delta_{(1,0)}^9 + \Delta_{(0,1)}^9)\phi(s_{i-1,j-1}) &= \frac{1}{43}\phi(s_{i-2,j-1}) + \frac{5}{174}\phi(s_{i-2,j}) + \frac{1}{43}\phi(s_{i-2,j+1}) + \frac{1}{43}\phi(s_{i-1,j-2}) \\
&+ \frac{5}{86}\phi(s_{i-1,j-1}) + \frac{5}{43}\phi(s_{i-1,j}) + \frac{5}{86}\phi(s_{i-1,j+1}) + \frac{1}{43}\phi(s_{i-1,j+2}) + \frac{5}{174}\phi(s_{i,j-2}) + \frac{5}{43}\phi(s_{i,j-1}) - \phi(s_{i,j}) \\
&+ \frac{5}{43}\phi(s_{i,j+1}) + \frac{5}{174}\phi(s_{i,j+2}) + \frac{1}{43}\phi(s_{i+1,j-2}) + \frac{5}{86}\phi(s_{i+1,j-1}) + \frac{5}{43}\phi(s_{i+1,j}) + \frac{5}{86}\phi(s_{i+1,j+1}) \\
&+ \frac{1}{43}\phi(s_{i+1,j+2}) + \frac{1}{43}\phi(s_{i+2,j-1}) + \frac{5}{174}\phi(s_{i+2,j}) + \frac{1}{43}\phi(s_{i+2,j+1}) \sim N(0, \kappa^{-1})
\end{aligned}$$

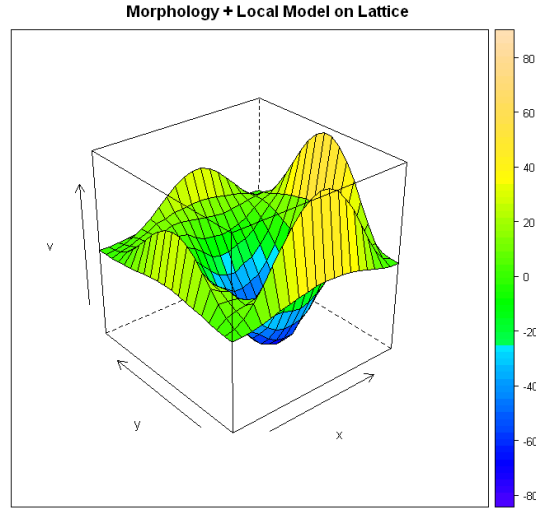


**Fig.15 Simulation for Increments from Spatial Statistics**

### 3.6 Summary

In this chapter, the morphology decomposition model was introduced and we focused on the local variability by specifying the interactions among the nanostructures. The Gaussian Markov random field was applied to model the morphology variation. The precision matrix played the central role in the random field. We constructed a precision matrix based on the conditional autoregression Gaussian scheme, the simultaneous autoregressive scheme and the increments. Finally the morphology variation was simulated based on the  $k^{th}$  order increments. This led to the intrinsic Gaussian Markov random field which is of practical use in the research work.

## Chapter 4

### Parameters Estimation for Nanowire Morphology Variation Model

The  $k^{th}$  order increments representation of neighborhood structures captures the interactions among different nanostructures in the same region on the substrate. The parameter estimation of the  $k^{th}$  order increments model is therefore critical to the nanostructure growth model described in Chapter 3. The spatial interactions of lattices have been researched for several decades and some related schemes and estimation methods have been developed. In this chapter, spatial interactions among nanostructures are to be estimated by maximum likelihood estimation (MLE).

#### 4.1 Autoregressive Scheme

Assume we have an infinite lattice of the local variability  $\phi(s_i)$  at the site of  $s_i$ , each site of which is normally distributed.

For one site  $\phi(s_i)$ , we have [69]:

$$E(\phi(s_i) | \phi(s_{-i})) = \mu_i + \sum \beta_{i,j} (\phi(s_j) - \mu_j) \quad (4.1)$$

Where,  $s_{-i}$  represents all the other sites except  $s_i$ ,  $\mu_i$  and  $\mu_j$  are the mean value of  $\phi(s_i)$  and  $\phi(s_j)$ ,  $\beta_{i,j}$  is 0 when  $\phi(s_i)$  and  $\phi(s_j)$  are local variabilities in different neighborhood structures.

Equation (4.1) can be written in the form of simultaneous autoregressive scheme,

$$\phi(s_i) = \mu_i + \sum \beta_{i,j} (\phi(s_j) - \mu_j) + \varepsilon_i \quad (4.2)$$

When the mean value of the site over the lattice is zero, the above equation will become,

$$\phi(s_i) = \sum \beta_{i,j} \phi(s_j) + \varepsilon_i \quad (4.3)$$

The error item  $\varepsilon_i$  is the same as the increment stated in Chapter 3. Then the estimation will be the fitting of the unknown parameters in equation (4.3), when the neighborhood structure is defined by the increment from the above equation.

#### 4.2 Simultaneous Autoregressive Scheme and the Increments

As stated above, the error term in Gaussian schemes are eventually the same as the increments which are fundamental in constructing a precision matrix for intrinsic Gaussian Markov Random Fields.

For example, the second order increment in constructing a precision matrix for intrinsic Gaussian Markov Random Field about the local nanostructure morphology variation is

$$(\Delta_{i,(1,0)}^2 + \Delta_{i,(0,1)}^2)\phi(s_{i-1,j-1}) = \phi(s_{i,j}) - \beta_{1,0}\phi(s_{i+1,j}) - \beta_{-1,0}\phi(s_{i-1,j}) - \beta_{0,1}\phi(s_{i,j+1}) - \beta_{0,-1}\phi(s_{i,j-1}) \sim N(0, \kappa^{-1}) \quad (4.4)$$

While the error term in the second-order Gaussian simultaneous autoregressive scheme is

$$\varepsilon_{i,j} = \phi(s_{i,j}) - \beta_{1,0}\phi(s_{i+1,j}) - \beta_{-1,0}\phi(s_{i-1,j}) - \beta_{0,1}\phi(s_{i,j+1}) - \beta_{0,-1}\phi(s_{i,j-1}) \sim N(0, \kappa^{-1}) \quad (4.5)$$

It is obvious that to estimate the coefficient in the increments is to estimate the parameters in the error term in Gaussian simultaneous autoregressive scheme.

#### 4.3 Maximum-Likelihood Estimation for Autoregressive Schemes

We begin by considering the estimation of the parameters in an auto-normal scheme of the form (4.1) but subject to the restriction  $\boldsymbol{\mu} = \mathbf{0}$ . We assume that the dimensionality of the parameter space is reduced through  $\boldsymbol{Q}$  having a particular structure and that is both unknown and independent of all the  $\beta_{i,j}$ .  $\boldsymbol{Q}$  is the  $n \times n$  matrix, whose diagonal elements are unity and whose off-diagonal  $(i, j)$  element is  $-\beta_{i,j}$ . For a given realization  $\mathbf{x}$ , the corresponding likelihood function is then equal to

$$(2\pi\sigma^2)^{-\frac{1}{2}n} |\boldsymbol{Q}|^{\frac{1}{2}} \exp\left(-\frac{1}{2}\sigma^{-2}\boldsymbol{\varphi}(\mathbf{s})^T \boldsymbol{Q}\boldsymbol{\varphi}(\mathbf{s})\right) \quad (4.6)$$

It follows that the maximum-likelihood estimate of  $\kappa^{-1}$  will be given by [69]

$$\kappa^{-1} = \mathbf{n}^{-1} \varphi(\mathbf{s})^T \mathbf{Q} \varphi(\mathbf{s}) \quad (4.7)$$

Once  $\hat{\mathbf{Q}}$ , the maximum-likelihood estimate of  $\mathbf{Q}$ , has been found, by substituting (4.7)

to (4.6), we find that  $\hat{\mathbf{Q}}$  can be found by minimizing

$$-n^{-1} \ln |\mathbf{Q}| + \ln(\varphi(\mathbf{s})^T \mathbf{Q} \varphi(\mathbf{s})) \quad (4.8)$$

Suppose then that we temporarily abandon the auto-normal model above and decide instead to fit a simultaneous scheme of the form (4.2), again subject to  $\boldsymbol{\mu} = \mathbf{0}$  and with  $\mathbf{Q}$  having the same structure as in (4.6). Provided (4.6) is valid, so is the present, but different, scheme. The likelihood function now becomes

$$(2\pi\sigma^2)^{-\frac{1}{2}n} |\mathbf{Q}| \exp\left(-\frac{1}{2} \sigma^{-2} \varphi(\mathbf{s})^T \mathbf{Q}^T \mathbf{Q} \varphi(\mathbf{s})\right) \quad (4.9)$$

and the new estimate of  $\mathbf{Q}$  must be found by minimizing

$$-n^{-1} \ln |\mathbf{Q}| + \ln(\varphi(\mathbf{s})^T \mathbf{Q}^T \mathbf{Q} \varphi(\mathbf{s})) \quad (4.10)$$

The only real difficulty centers upon the evaluation of the determinant  $|\mathbf{Q}|$ , we may use the semi-analytical result of Whittle [70].

To minimize (4.8), where  $n^{-1} \ln |\mathbf{Q}|$  is the absolute term in the power series expansion of

$$\ln(1 - \sum \sum \beta_{k,l} z_1^k z_2^l) \quad (4.11)$$

and where, neglecting boundary effects,

$$\varphi(\mathbf{s})^T \mathbf{Q} \varphi(\mathbf{s}) = C_{0,0} - \sum \sum \beta_{k,l} C_{k,l} \quad (4.12)$$

and  $C_{k,l}$  denotes the empirical autocovariance of lags  $k$  and  $l$  in  $i$  and  $j$ , respectively.

Let us suppose we have a set of data on a regular lattice of the local variability of nanostructures, namely  $\phi(s_{i,j})$  ( $i = 1, 2, \dots, m; j = 1, 2, \dots, n$ ), so the empirical

covariance of lag  $k$ ,  $l$  is

$$C_{k,l} = \frac{1}{mn} \sum_{i=1}^{m-k} \sum_{j=1}^{n-l} \phi(s_{i,j}) \phi(s_{i+k,j+l}) \quad (4.13)$$

The absolute term in the power series expansion can easily be evaluated for given parameters by appropriate numerical Fourier inversion. For the following scheme

$$\phi(s_{i,j}) = \alpha + \beta_1 \phi(s_{i-1,j}) + \beta_1 \phi(s_{i+1,j}) + \beta_2 \phi(s_{i,j-1}) + \beta_2 \phi(s_{i,j+1}) \quad (4.14)$$

The absolute term in  $\ln\{1 - \beta_1(z_1 + z_1^{-1}) - \beta_2(z_2 + z_2^{-1})\}$  will be

$$-\Lambda(\bar{\beta}) = \frac{1}{2} \sum_{j=1}^{\infty} \sum_{k=0}^j \frac{(2j)!}{j![k!(j-k)!]^2} \beta_1^{2k} \beta_2^{2(j-k)} \quad (4.15)$$

Thus we will minimize

$$-\Lambda(\bar{\beta}) + \ln(C_{0,0} - 2\beta_1 C_{1,0} - 2\beta_2 C_{0,1}) \quad (4.16)$$

For another conditional autoregressive scheme

$$\phi(s_{i,j}) = \alpha + \beta_{-1,0} \phi(s_{i-1,j}) + \beta_{1,0} \phi(s_{i+1,j}) + \beta_{0,1} \phi(s_{i,j-1}) + \beta_{0,-1} \phi(s_{i,j+1}) \quad (4.17)$$

the following function will be minimized to get the parameters

$$-\Lambda(\beta) + \ln(C_{0,0} - \beta_{-1,0} C_{1,0} - \beta_{1,0} C_{1,0} - \beta_{0,1} C_{0,1} - \beta_{0,-1} C_{0,1}) \quad (4.18)$$

The absolute term in  $\ln(1 - \beta_{-1,0} z_1 - \beta_{1,0} z_1^{-1} - \beta_{0,-1} z_2 - \beta_{0,1} z_2^{-1})$  will be

$$-\Lambda(\beta) = \frac{1}{2} \sum_{j=1}^{\infty} \sum_{k=0}^j \frac{(2j)!}{j![k!(j-k)!]^2} (\beta_{1,0} \beta_{-1,0})^k (\beta_{0,1} \beta_{0,-1})^{(j-k)} \quad (4.19)$$

The second order conditional autoregression scheme is

$$\begin{aligned} \phi(s_{i,j}) = & \alpha + \beta_1 (\phi(s_{i-1,j}) + \phi(s_{i+1,j})) + \beta_2 (\phi(s_{i,j-1}) + \phi(s_{i,j+1})) + \beta_3 (\phi(s_{i-1,j-1}) \\ & + \phi(s_{i+1,j+1})) + \beta_4 (\phi(s_{i-1,j+1}) + \phi(s_{i+1,j-1})) \end{aligned} \quad (4.20)$$

For scheme (4.20), we will minimize

$$-\Lambda(\beta) + \ln(C_{0,0} - 2\beta_1 C_{1,0} - 2\beta_2 C_{0,1} - 2\beta_3 C_{1,1} - 2\beta_4 C_{1,-1}) \quad (4.21)$$

Cressie [64] made his comment on the Whittle's approximation and Whittle's poor fit of spatial models to the Mercer and Hall data (1911). In his opinion, Whittle's

fail would be due to the inconsistent likelihood approximation chosen and more due to his not accounting for the large-scale variation (trend) in the data. While for the data in our model, the trend part is excluded by the profile of the morphology.

It is noticeable that the increments in defining the intrinsic GMRFs in Chapter 3 are equivalent to the error terms in simultaneous autoregressive Gaussian schemes, and the minimization of equation (4.8) is for auto-normal schemes. It is also proved that the auto-normal schemes and the simultaneous autoregressive Gaussian schemes are reciprocally transformable. For auto-normal scheme (4.16), the simultaneous autoregressive Gaussian scheme when the global mean is equal to zero is

$$\phi(s_{i,j}) = \beta_1\phi(s_{i-1,j}) + \beta_1\phi(s_{i+1,j}) + \beta_2\phi(s_{i,j-1}) + \beta_2\phi(s_{i,j+1}) + \varepsilon_{i,j} \quad (4.22)$$

The result from minimizing equation (4.16) also matches equations (4.22), which is equivalent to the increments in defining GMRFs when equation (4.22) is rewritten as

$$\phi(s_{i,j}) = \phi(s_{i,j}) - a\phi(s_{i-1,j}) - a\phi(s_{i+1,j}) - b\phi(s_{i,j-1}) - b\phi(s_{i,j+1}) \quad (4.23)$$

#### 4.4 Coding Methods on Lattice

Besag (1974) introduced coding methods on the rectangular lattice in the context of binary data and the methods are effective for more general situations.

In his methods, for example, to fit the first order scheme (4.14), the interior sites of the lattice is labeled alternatively by  $\cdot$  and  $+$ , as shown by Fig.16.

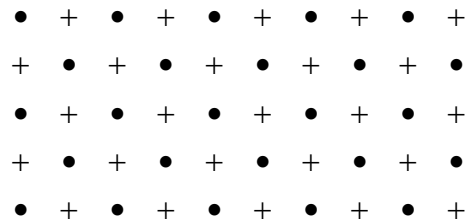


**Fig.16 Coding Pattern for a First-order Scheme**

Since the variables associated with the + sites, given all the other observations on the lattice, only depends on their immediate · sites, they are reciprocally independent. This will result in the conditional likelihood,

$$\prod p_{i,j}(\phi(s_{i,j}) | \phi(s_{i-1,j}), \phi(s_{i+1,j}), \phi(s_{i,j-1}), \phi(s_{i,j+1}))$$

The product is taken over all + sites. Conditional maximum likelihood estimates of the parameters in the scheme could be obtained following the procedures in the above section. The estimates of the same scheme could also be obtained by maximizing the likelihood function for the · sites conditional on the immediate + sites. The results from the two procedures can be different to some extent and it is better to combine the two results appropriately.

To fit a second-order scheme, for example scheme (4.20), the interior sites are labeled by · and + as shown in Fig.17.

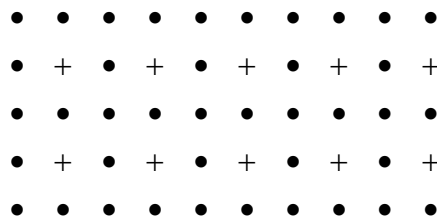


**Fig.17 Coding Pattern for a Second-order Scheme**

Unlike Fig.16, which could interpret the variables at both · and + sites, Fig.17 only interprets the joint distributions of the + site values given the · site values. When the joint distribution of all the + sites is obtained, we can estimate the unknown parameters by the methods introduced above. By performing shifts of the entire coding framework over the lattice, four sets of estimates are available and these results should be combined appropriately.

Parameter estimation under coding patterns would provide us with convenience of selecting data regions. The combinations of the estimated parameters under different coding patterns would approach the true interactions. We will use this method in future work.

#### 4.5 Parameter Estimation Method Using Simulation Data

To test the above estimation method, we will simulate a set of data from the given parameters and try to use that data to make estimations that will return to the original model.

Supposing infinite lattice of the local morphology variations  $\phi(s_{s,t})$  of nanostructures, the simulated data are from the following conditional autoregression scheme:

$$\phi(s_{i,j}) | \phi(s_{i-1,j}), \phi(s_{i+1,j}), \phi(s_{i,j-1}), \phi(s_{i,j+1}) = 0.3\phi(s_{i-1,j}) + 0.3\phi(s_{i+1,j}) + 0.2\phi(s_{i,j-1}) + 0.2\phi(s_{i,j+1})$$

where,  $\alpha = 0$ , meaning that the mean of local variability is zero. The mean will keep zero for the following cases, because the trend part is excluded by the profile of the global morphology determined by growth kinetics.

By the simulation method in Chapter 3, the simulated data (Data Set 3) is shown in Table 3.

**Table 3: Data Simulated from the Model with Given Parameters**

|        |        |        |        |        |        |        |        |         |        |
|--------|--------|--------|--------|--------|--------|--------|--------|---------|--------|
| 0.397  | 0.928  | 0.404  | -0.209 | -0.396 | -0.955 | -1.515 | -0.931 | 0.6047  | 0.277  |
| 1.107  | 1.297  | 2.939  | 1.409  | 1.546  | -1.166 | -2.503 | -1.758 | -0.3305 | 0.092  |
| 2.200  | 2.338  | 1.620  | 0.598  | -0.645 | -0.033 | 0.517  | -0.891 | -2.3252 | -0.699 |
| 1.457  | 0.784  | -0.605 | 0.410  | -1.402 | -2.263 | -1.967 | -1.420 | -0.8909 | -1.315 |
| 1.271  | 0.064  | -1.277 | 0.101  | -1.150 | -0.267 | -0.709 | -0.926 | 1.3963  | 0.365  |
| -1.594 | 0.643  | 1.016  | -1.544 | -1.514 | -1.066 | 2.611  | 1.098  | 1.8450  | 1.820  |
| -0.932 | -0.458 | -2.492 | -2.065 | -0.716 | 0.439  | 2.837  | 0.156  | -1.3642 | 0.954  |
| -2.281 | -1.834 | -2.197 | -1.940 | 0.426  | 1.616  | 1.803  | 0.836  | -0.6537 | 0.339  |
| 0.782  | -1.386 | -0.785 | -2.756 | 0.534  | 1.364  | 1.415  | -0.830 | 0.8775  | 0.936  |
| -0.602 | -0.969 | -0.598 | -1.120 | 3.341  | 1.536  | 1.531  | 0.125  | 0.1044  | 0.300  |

The model to be estimated should have the same form,

$$\phi(s_{i,j}) = \beta_{1,0}\phi(s_{i-1,j}) + \beta_{-1,0}\phi(s_{i+1,j}) + \beta_{0,1}\phi(s_{i,j-1}) + \beta_{0,-1}\phi(s_{i,j+1})$$

By the maximum likelihood estimation, we can have the estimated results shown in Table 4 by maximum-likelihood estimation (MLE) method, because the interactions to the left and to the right are assumed to be the same.

**Table 4: Parameters Estimation for Data Set 3 by MLE**

|            |               |               |
|------------|---------------|---------------|
| Parameters | $\beta_{1,0}$ | $\beta_{0,1}$ |
| Values     | 0.2723        | 0.2334        |

The above results are obtained by adding 1.5 global mean to the data in Table 3. If we compare the estimated results with the given parameters, we have confidence that the estimation method is of relatively good accuracy.

#### 4.6 Model Estimation for Two Sets of Real Data

From the observations of scanning electron microscopy, we collected two sets of data concerning the lengths of nanowires which are shown in the figures in Chapter 2. According to the two sets of data, we could have the parameter estimated by the maximum likelihood estimation method.

For the first set of data, we at the beginning fit it as the conditional autoregressive scheme of the first order, which is the same as scheme (4.14)

$$\phi(s_{i,j}) = \beta_{1,0}\phi(s_{i+1,j}) + \beta_{1,0}\phi(s_{i-1,j}) + \beta_{0,1}\phi(s_{i,j-1}) + \beta_{0,1}\phi(s_{i,j+1})$$

In this case the interactions in the horizontal direction are the same, no matter whether the neighboring site is in the left or in the right. The interactions in the vertical direction are identified as well. The estimated parameters are shown in Table 5 by MLE method.

**Table 5: Parameters Estimation for Data Set 1 by MLE**

|            |               |               |
|------------|---------------|---------------|
| Parameters | $\beta_{1,0}$ | $\beta_{0,1}$ |
| Values     | 0.1049        | 0.1119        |

From the results, we can tell that the vertical interaction is larger than the interaction in the horizontal direction.

Then we fit the first set of data as another conditional autoregressive scheme of the first order, which is the same as scheme (4.17)

$$\phi(s_{i,t}) = \beta_{-1,0}\phi(s_{i-1,j}) + \beta_{1,0}\phi(s_{i+1,j}) + \beta_{0,-1}\phi(s_{i,j-1}) + \beta_{0,1}\phi(s_{i,j+1})$$

In this case the interactions of the immediate neighbors in the horizontal direction could be different. The interactions in the vertical direction are fluctuant as well. The estimated parameters are shown in Table 6 by MLE method.

**Table 6: Parameters Estimation for  
Data Set 1 by MLE**

| Parameters | $\beta_{-1,0}$ | $\beta_{1,0}$ | $\beta_{0,-1}$ | $\beta_{0,1}$ |
|------------|----------------|---------------|----------------|---------------|
| Values     | -0.4463        | 0.3924        | 0.3196         | 0.3964        |

From Table 6 we could have the conclusion that the interactions of the coming sites are generally larger than those of the past sites. By comparing the results in Table 6 with the results in Table 5, we could find the differences between the two results are relatively large, due to the different scheme used in the model. It should be concluded that the appropriate model, for instance, the right order and the accurate interactions, needs to be tried more times.

For the second set of data, to validate the parameters we obtained above, we also fit it as the conditional autoregressive scheme of the first order, which is the same as scheme (4.14)

$$\phi(s_{i,j}) = \beta_{1,0}\phi(s_{i-1,j}) + \beta_{1,0}\phi(s_{i+1,j}) + \beta_{0,1}\phi(s_{i,j-1}) + \beta_{0,1}\phi(s_{i,j+1})$$

It is the same case that the interactions in the horizontal direction are the same, no matter whether the neighboring site is in the left or in the right. The interactions in the vertical direction are identified as well. The estimated parameters are shown in Table 7 by MLE method.

**Table 7: Parameters Estimation for  
Data Set 2 by MLE**

|            |               |               |
|------------|---------------|---------------|
| Parameters | $\beta_{1,0}$ | $\beta_{0,1}$ |
| Values     | -0.0198       | 0.1067        |

From the results, we can tell that the vertical interaction is much larger than the interaction in the horizontal direction.

Then we fit the first set of data as another conditional autoregressive scheme of the first order, which is the same as scheme (4.17)

$$\phi(s_{i,t}) = \beta_{-1,0}\phi(s_{i-1,j}) + \beta_{1,0}\phi(s_{i+1,j}) + \beta_{0,-1}\phi(s_{i,j-1}) + \beta_{0,1}\phi(s_{i,j+1})$$

It is obvious that the interactions of the immediate neighbors in the horizontal direction could be different. The interactions in the vertical direction are fluctuant as well. The estimated parameters are shown in Table 8 by MLE method.

**Table 8: Parameters Estimation for  
Data Set 2 by MLE**

|            |                |               |                |               |
|------------|----------------|---------------|----------------|---------------|
| Parameters | $\beta_{-1,0}$ | $\beta_{1,0}$ | $\beta_{0,-1}$ | $\beta_{0,1}$ |
| Values     | 0.4164         | -0.3989       | 0.4989         | 0.2620        |

It is noticeable that the summation of the parameters would be around 1, which is an intrinsic requirement. Therefore it is needed to adjust the parameters to make their summation close to 1. By comparing the estimation results and the validation results, we could find that the interactions for different regions could be significantly different. It is reasonable that the differences between two close and similar regions are smaller, as shown in Table 8. The results from the first and the second analysis are similar while those from the third and the fourth analysis are close. However, the differences between them are relatively large. The possible reason could be: a) the data are collected in the different regions of the same substrate and therefore it is very likely that the interactions are of great difference; b) the measurement method of the nanowires contains simplifications and assumptions for the sake of fast computation and the size of data is not big enough; c) the first-order model may not be the best for estimating the parameters for the interactions among the lengths of the nanowires, so complicated model will be conducted later in the research work.

For a higher order scheme, the process is the same as the first-order examples stated above. The computation might be time-consuming and the coding pattern needs to be expanded by shifting the entire framework for more times.

#### **4.7 Summary**

In this chapter, parameter estimation and validation for the nanostructure morphology variation model have been accomplished using the maximum likelihood estimation. The conditional autoregression scheme and the simultaneous autoregressive scheme are introduced to construct the conditional and joint probability models. A test is conducted to prove the feasibility of the method. Then parameter estimation is done on the two sets of the obtained data, the later one of which is for validation. After the numerical examples, it is found that the differences between the

estimation results and the validation results are relatively large. The possible reasons are possibly due to the different regions from where the two sets of data are collected, the inaccuracy in the measurement and the improper neighborhood structure in the model selected.

## Chapter 5

### Conclusions

In this research, a series study was carried out on nanostructure morphology variation modeling and estimation for nanomanufacturing process yield improvement. The following goals were achieved: a). A simplified method was proposed for measuring nanowire lengths from scanning electron microscopy images; b). ZnO nanowire morphology variation modeling was built using Gaussian Markov Random Fields and various simulations were accomplished to form morphology library; c). Parameter estimation and validation for the model were accomplished for the collected data.

Firstly, through a systematic investigation on the three-dimensional scanning electron microscopy images, a simplified method for measuring ZnO nanowire length from two SEM images obtained from two different angles was developed. The measurement method follows the principles of Photogrammetry and the two SEM images are achieved by tilting the rotational axis at a given degree of angle.

Secondly, ZnO nanowire morphology variation models were set up by Gaussian Markov Random Fields (GMRFs). Nanostructure morphology variation modeling is a typically spatial data analysis. In this thesis, the spatial data of ZnO length all over the substrate at a given time was studied by GMRFs. The sampling algorithm concentrates more on precision matrix, which is a key feature for GMRFs. A library of morphology has been set up based on various neighborhood structure.

Thirdly, parameter estimation and validation for the nanostructure morphology variation model was accomplished based on the two sets of collected data using the

maximum likelihood estimation method. We estimated the parameters in two first-order conditional autoregression schemes for both of the two sets. In the first scheme the interactions in the horizontal direction are the same and the interactions in the vertical direction are identical as well, however the interactions in both directions could be different. In the other scheme, all the interactions between the four immediate neighbors and the central site could be fluctuant. From the results, we know both of the estimation results and the validation results show the same tendency of the interactions. The interactions in the horizontal direction are less than the interactions in the vertical direction. However, the differences between them are relatively large, possibly due to the different regions from where the two sets of data are collected, the inaccuracy in the measurement and the improper neighborhood structure in the model selected. The higher order will be studied following the same procedures and better neighborhood structure for the nanostructures could be obtained at higher orders.

## References

- [1] P. K. Sekhar., 2008, “Nanomanufacturing of Silica Nanowires: Synthesis, Characterization and Applications”, Ph.D. Dissertation, University of South Florida
- [2] <http://www.understandingnano.com/introduction.html>
- [3] P. X. Gao, 2005, “Piezoelectric Nanostructures of Zinc Oxide: Synthesis, Characterization and Devices”, Ph.D. Dissertation, Georgia Institute of Technology
- [4] R. Abdelali, B. Magali, and B. Claude, 2003, “Signature of small rings in the Raman spectra of normal and compressed amorphous silica”, *Physical Review B*, 68, 184202
- [5] Y. Maruyama, and M. Futamata, 2005, “Elastic scattering and emission correlated with single-molecule SERS”, *Journal of Raman Spectroscopy*, 36, 581
- [6] A.D. McFarland, M.A.Young, J.A. Dieringer and R.P Van Duyne, 2005, “Wavelength-Scanned Surface-Enhanced Raman Excitation Spectroscopy” *Journal of Physical Chemistry B*, 109, 11279
- [7] V. N. Pustovit and T. V. Shahbazyan, 2006, “Surface-enhanced Raman scattering on the nanoscale: a microscopic approach”, *Journal of Optics. A: Pure and Applied optics*, 8, S208
- [8] P.K.Sekhar, N.S.Ramgir, R.K.Joshi and S.Bhansali, 2008, “Selective growth of silica nanowires using Au catalyst for optical recognition of Interleukin-10”, *Nanotechnology*, 19, 255502.
- [9] L. A. Bauer, N. S. Birenbaum and G. J. Meyer, 2004, “Biological Applications of High Aspect Ratio Nanoparticles”, *Journal of Materials Chemistry*, 14, 517.
- [10] M. Paulose, O.K. Vargheese and C.A. Grimes, 2003, “Synthesis of Gold-Silica Composite Nanowires through Solid-Liquid-Solid Phase Growth”, *Journal of Nanoscience and Nanotechnology*, 3, 341
- [11] P. Kask, K. Palo, D. Ullmann and K. Gall, 1999, “Fluorescence-intensity distribution analysis and its application in biomolecular detection technology”, *PNAS*, 96, 13756
- [12] J.B. Hannon, S. Kodambaka, F.M.Ross, and R.M. Tromp, 2006, “The influence of the surface migration of gold on the growth of silicon nanowires”, *Nature*, 440, 69.
- [13] K.W. Kolasinski, 2006, “Catalytic growth of nanowires: Vapor–liquid–solid, vapor–solid–solid, solution–liquid–solid and solid–liquid–solid growth”, *Current Opinion in Solid State and Materials Science*, 10, 182

- [14] W. Lu and C.M. Lieber, 2006, "Semiconductor nanowires", *Journal of Physics. D: Applied Physics*, 39, R387.
- [15] F.Gao, 2004, "Clay/Polymer Composites: The Theory", *Materials Today*, 7, 50.
- [16] V.P.Veedu, A.Cao, X.Li, K.Ma, C.Soldano, S.Kar, P.A.Ajayan and M.N. G Nejhada, 2006, "Multifunctional Composites using Reinforced Laminate with Carbon Nanotube Forests", *Nature Materials*, 5, 457.
- [17] M.J.A. de Dood, J. Knoester, A. Tip and A. Polman, 2005, "Förster transfer and the local optical density of states in erbium-doped silica", *Physical Review B*, 71, 5.
- [18] E. Snoeks, A. Lagendijk and A.Polman, 1995, "Measuring and Modifying the Spontaneous Emission Rate of Erbium near an Interface", *Physical Review Letters*, 74, 2459
- [19] P.K.Sekhar, R.G. Elliman, A.R. Wilkinson, and S. Bhansali, 2008, "Enriched Er Emission from Nanoengineered Si Surface", *The Journal of Physical Chemistry C: Letters*, (In Print).
- [20] J.F.Ziegler, J.P.Biersack, and M.D.Ziegler, 2008, *The Stopping and Range of Ions in Matter*. Lulu Press
- [21] D. Dijkkamp, T. Venkatesan, D. Wu, S. A. Shaheen, N. Jisrawi, Y. H. Minlee, W. L. Mclean, M. Croft, 1987, "Preparation of Y-Ba-Cu oxide superconductor thin films using pulsed laser evaporation from high Tc bulk material", *Applied Physics Letters*, 51, 619.
- [22] J. C. Wang, S. Q. Feng, D. P. Yu, 2002, "High-quality GaN nanowires synthesized using a CVD approach", *Applied Physics A*, 75, 691.
- [23] Z. Zhong, F. Qian, D. Wang, C. M. Lieber, 2003, "Synthesis of p-type gallium nitride nanowires for electronic and photonic nanodevices", *Nano Letters*, 3, 343.
- [24] B. Zheng, C. Lu, G. Gu, A. Makarovski, G. Finkelstein and J. Liu, 2002, "Efficient CVD Growth of Single-Walled Carbon Nanotubes on Surfaces Using Carbon Monoxide Precursor", *Nano Letters*, 2, 895.
- [25] C. M. Hsu, C. H. Lin, H. J. Lai and C. T. Kuo, 2005, "Root growth of multi-wall carbon nanotubes by MPCVD", *Thin Solid Films*, 471, 140.
- [26] X. F. Duan and C. M. Lieber, 2000, "General Synthesis of Compound Semiconductor Nanowires", *Advanced Materials*, 12, 298.
- [27] Y. Cui, L. J. Lauhon, M. S. Gudixsen, J. Wang and C. M. Lieber, 2001, "Diameter-controlled synthesis of single-crystal silicon nanowires", *Applied Physics Letters*, 78, 2214.

- [28] X. F. Duan, C. M. Niu, V. Sahi, J. Chen, J. W. Parce, S. Empedocles and J. L. Goldman, 2003, "High-performance thin-film transistors using semiconductor nanowires and nanoribbons", *Nature*, 425, 274.
- [29] M. S. Gudiksen, L. J. Lauhon, J. F. Wang, D. C. Smith and C. M. Lieber, 2002, "Growth of nanowire superlattice structures for nanoscale photonics and electronics", *Nature*, 415, 617.
- [30] L.J. Lauhon, M.S. Gudiksen, D. Wang, and C.M. Lieber, 2002, "Epitaxial core-shell and core-multishell nanowire heterostructures", *Nature*, 420, 57.
- [31] Y. H. Kim, J. Y. Lee, S. H. Lee, J. E. Oh, H. S. Lee, 2005, "Synthesis of aligned GaN nanorods on Si (111) by molecular beam epitaxy", *Applied Physics A*, 80,1635.
- [32] H. Hasegawa, S. Kasai, 2001, "Hexagonal binary decision diagram quantum logic circuits using Schottky in-plane and wrap-gate control of GaAs and InGaAs nanowires", *Physica E*, 11, 149.
- [33] Z. H. Wu, M. Sun, Y. Mei, H. E. Ruda, 2004, "Growth and photoluminescence characteristics of AlGaAs nanowires", *Applied Physics Letters*, 85, 657.
- [34] Y. S. Min, E. J. Bae, K. S. Jeong, Y. J. Cho, J. H. Lee, W. B. Choi, G. S. Park, 2003, "Ruthenium Oxide Nanotube Arrays Fabricated by Atomic Layer Deposition Using a Carbon Nanotube Template", *Advanced Materials*,15, 1019.
- [35] M. S. Sander, M. J. Cote, W. Gu, B. M. Kile, C. P. Tripp, 2004, "Template-Assisted Fabrication of Dense, Aligned Arrays of Titania Nanotubes with Well-Controlled Dimensions on Substrates", *Advanced Materials*, 16, 2052.
- [36] H. Shin, D. K. Jeong, J. Lee, M. M. Sung, J. Kim, 2004, "Formation of TiO<sub>2</sub> and ZrO<sub>2</sub> Nanotubes Using Atomic Layer Deposition with Ultraprecise Control of the Wall Thickness", *Advanced Materials*, 16, 1197.
- [37] X. D. Wang, E. Graugnard, J. S. King, Z. L. Wang, and C. J. Summers, 2004, "Large-Scale Fabrication of Ordered Nanobowl Arrays", *Nano Letters*, 4, 2223.
- [38] J.J. Urban, W.S. Yun, Q. Gu, H. Park, 2002, "Synthesis of Single-Crystalline Perovskite Nanorods Composed of Barium Titanate and Strontium Titanate", *Journal of the American Chemical Society*, 124, 1186.
- [39] J.J. Urban, J. E. Spanier, O. Y. Lian, W.S. Yun, H. Park, 2003, "Single-Crystalline Barium Titanate Nanowires", *Advanced Materials*.,15, 423.
- [40] R. S. Wager, W. C. Ellis, 1964, "Vapor-liquid-solid mechanism of single crystal growth", *Applied Physics Letters*, 4, 89
- [41] A.A. Chernov, "Growth kinetics and capture of impurities during gas phase crystallization", 1977, *Journal of Crystal Growth*, 42,55

- [42] E.I. Givargizov, 1975, "Fundamental Aspects of VLS Growth", *Journal of Crystal Growth*, 31, 20
- [43] McIlroy, D.N., A. Alkhateeb, D. Zhang, D.E. Aston, A.C. Marcy, M. Grant Norton, 2004, "Nanospring Formation: Unexpected Catalyst Mediated Growth", *Journal of Physics Condensed Matter*, 16, R415.
- [44] V. G. Dubrovskii and N. V. Sibirev, 2004, "Growth rate of a crystal facet of arbitrary size and growth kinetics of vertical nanowires", *Physics Review E*, 70, 031604
- [45] V.G. Dubrovskii, I.P. Soshnikov, N.V. Sibirev, G.E. Cirlin and V.M. Ustinov, 2006, "Growth of GaAs nanoscale whiskers by magnetron sputtering deposition", *Journal of Crystal Growth*, 289, 31-36
- [46] V.G. Dubrovskii, N.V. Sibirev and G.E. Cirlin, 2004, "Kinetic Model of the Growth of Nanodimensional Whiskers by the Vapor-Liquid-Crystal Mechanism", *Technical Physics Letters*, 30, 4-50
- [47] D.Kashchiev, 2000, *Nucleation: Basic Theory with Applications*, Butterworth Heinemann. Oxford
- [48] W.Obretenov, D.Kashchiev, V.Bostanov, 1989, "Unified description of the rate of nucleation-mediated crystal growth", *Journal of crystal growth*, 96,843
- [49] V. Ruth and J.P. Hirth, 1964, "Kinetics of Diffusion-Controlled Whisker Growth", *Journal of Chemical Physics*, 10, 3139
- [50] J. Kikkawa, Y. Ohno, and S. Takeda, 2005, "Growth rate of silicon nanowires", *Applied Physics Letters*, 86, 12109
- [51] *Societal Implications of Nanoscience and Nanotechnology*. Arlington, VA: National Science Foundation, 2001
- [52] Michael T. Postek, "Nanometrology: Fundamental for Realizing Products at the Nanoscale", 2007
- [53] *2005 NCMS Survey of Nanotechnology in the U.S. manufacturing Industry*. Ann Arbor, MI: National Center for Manufacturing Science, 2006
- [54] *Implications of Emeerging Micro- and Nanotechnologies*. Washington DC:The National Academies Press, 2002
- [55] W. Kuo, 2006, "Challenges related to reliability in nano electronics", *IEEE Transactions on Reliability*, 55, 569
- [56] G. Piazzesi, 1973, "Photogrammetry with the scanning electron microscope", *Journal of Physics E: Scientific Instruments.*, 6, 392

- [57] P. Bariani, L. De Chiffre, H.N. Hansen, A. Horsewell, 2005, "Investigation on the traceability of three dimensional scanning electron microscope measurements based on the stereo-pair technique", *Precision Engineering*, 29, 219–228
- [58] T. Dasgupta, C. Ma, V. R. Joseph, Z. L. Wang, and C. F. Wu, 2008, "Statistical modeling and analysis for robust synthesis of nanostructures", *Journal of the American Statistical Association*, 103, 594
- [59] W. Luo, Y. Kuo, and W. kuo, 2004, "Dielectric relaxation and breakdown detection of doped tantalum oxide high-k thin film", *IEEE Transaction on Device and Materials Reliability*, 4, 488
- [60] W. Luo, T. Yuan, Y. Kuo, J. Yan, and W. Kuo, 2006, "Breakdown phenomena of zirconium-doped hafnium oxide high-k stack with an inserted interface layer", *Applied Physics Letters*, 89, 072901
- [61] S. J. Bae, S. J. kim, W. Kuo, and Kvam, 2007, "Statistical Models for hot electron degradation in nano-scaled mosfet devices", *IEEE Transactions on Reliability*, 56, 392
- [62] Q. Huang, 2009, "Physics-driven Bayesian hierarchical modeling of nanowire growth process", *IIE Transactions*, Under revision.
- [63] B. Ripley, 1981, *Spatial Statistics*. John Wiley & Sons, 1981
- [64] N. Cressie, 1993, *Statistics for Spatial Data, revised edition ed.* John Wiley & Sons
- [65] V. R. Joseph, Y. Hung and A. Sudjianto, 2008, "Blind kriging: A blind kriging: A new method for developing metamodels", *ASME Journal of Mechanical Design*, 130, 031102
- [66] H. Rue and L. Held, 2005, *Gaussian Markov Random Fields: Theory and Applications*. Chapman & Hall/CRC, 2005
- [67] H. Rafii-Tabar, 2008, *Computational Physics of Carbon Nanotubes*. Cambridge University Press,
- [68] L. E. Lennard-Jones, 1924, "On the determination of molecular fields. ii. from the equation of state of a gas", *Proceedings of the Royal Society of London-Series A*, 106, 463
- [69] J. Besag, 1974, "Spatial Interaction and the Statistical Analysis of Lattice Systems", *Journal of the Royal Statistical Society. Series B (Methodological)*, 36, 192
- [70] P. Whittle, 1954, "Stationary Processes in the Plane", *Biometrika*, 41, 434